catalysts

MDPI

Review

Main Hydrogen Production Processes: An Overview

Marco Martino [1,*], Concetta Ruocco [1], Eugenio Meloni [1], Pluton Pullumbi [2] and Vincenzo Palma [1]

[1] Department of Industrial Engineering, University of Salerno, Via Giovanni Paolo II 132, 84084 Fisciano, SA, Italy; cruocco@unisa.it (C.R.); emeloni@unisa.it (E.M.); vpalma@unisa.it (V.P.)
[2] Air Liquide, Paris Innovation Campus. 1, Chemin de la Porte des Loges, 78350 Les Loges en Josas, France; pluton.pullumbi@airliquide.com
* Correspondence: mamartino@unisa.it; Tel.: +39-089-964027

Abstract: Due to its characteristics, hydrogen is considered the energy carrier of the future. Its use as a fuel generates reduced pollution, as if burned it almost exclusively produces water vapor. Hydrogen can be produced from numerous sources, both of fossil and renewable origin, and with as many production processes, which can use renewable or non-renewable energy sources. To achieve carbon neutrality, the sources must necessarily be renewable, and the production processes themselves must use renewable energy sources. In this review article the main characteristics of the most used hydrogen production methods are summarized, mainly focusing on renewable feedstocks, furthermore a series of relevant articles published in the last year, are reviewed. The production methods are grouped according to the type of energy they use; and at the end of each section the strengths and limitations of the processes are highlighted. The conclusions compare the main characteristics of the production processes studied and contextualize their possible use.

Keywords: hydrogen; reforming; gasification; water splitting; dark-fermentation; photo-fermentation; CO gas-fermentation; bio-photolysis; electrolysis

Citation: Martino, M.; Ruocco, C.; Meloni, E.; Pullumbi, P.; Palma, V. Main Hydrogen Production Processes: An Overview. *Catalysts* **2021**, *11*, 547. https://doi.org/10.3390/catal11050547

Academic Editor: Binlin Dou

Received: 7 April 2021
Accepted: 24 April 2021
Published: 25 April 2021

1. Introduction

In 2012 the UN Secretary-General stated that 'Energy is the Golden Thread', which connects economic growth, social equity, and environmental sustainability [1]. After more than 8 years, still today a significant percentage of the world population lives in conditions of energy poverty, and a large portion depends on highly polluting fuels and technologies [2]. The 2018 Intergovernmental Panel on Climate Change (IPCC) special report [3] on the impacts of global warming of 1.5 °C above pre-industrial levels and on the effects of global greenhouse gas emissions (GHG), has pointed out the need to drastically reduce these emissions. To effectively counteract the climate change, greenhouse gas emissions need to be reduced by at least 45% by 2030 [4], and carbon neutrality reached by 2050 [5] to stay below +1.5 °C of global warming. Therefore, we have two challenges ahead of us, we need more energy, but it has to be clean energy. Despite a wide variety of energy sources, fossil fuels (coal, oil and natural gas) still provide most of the energy needed to support human activities [6], but to achieve carbon neutrality the sources can only be renewable; therefore, it is necessary to reduce the consumption of fossil sources. Hydrogen is not a primary source but an energy vector [7], however some characteristics make it an extremely attractive candidate for making an energy transition to renewable sources. Hydrogen has been discovered for more than three hundred years [7,8], it is the most abundant element in the universe [9]; hydrogen can be produced from a wide range of technical processes and feedstocks, both fossil fuels, i.e., non-renewable source, and renewable sources such as biomass, moreover it is not toxic and it has heating values of 2.4, 2.8 and 4 times higher than those of methane, gasoline and coal, respectively [10]. Biomass is considered a promising source for hydrogen production (the hydrogen content in biomass is ~5–7 wt%), as a CO_2 neutral precursor, although the carbon footprint, in using biomass,

is not effectively neutral [11]. It has been reported that 8.99×10^{-2} eqv·g·s^{-1} of CO_2 are emitted to produce 0.484 MJ·s^{-1} of hydrogen from 2.53×10^6 kg of biomass [11]. One of the critical aspects in the use of biomass is associated with land consumption, however alternatives like lignocellulosic, crops and organic waste sewage sludge, biooil, and biochar can be used as alternative. The nature and the availability of the feedstock is just one of the critical parameters, in the choice of the best process to be used, the energy required to sustain the process and the eventual use of catalysts, are equally crucial [12]. Different types and combinations of energy can be used, included thermal, electrical, bioenergy and photonic. The renewability of energy sources is another critical parameter, and plays a fundamental role, in the choice of the processes that will lead us to carbon neutrality.

This review aims to provide an overview of the major hydrogen production processes, mainly but not only focusing on those that make use of renewable sources, moreover for each process some relevant articles published in the last year are reviewed.

2. Thermal Methods

Currently, most hydrogen is produced by thermal processes, including reforming, gasification, and thermochemical methods. In the next sections a general overview of the main process will be provided.

2.1. Steam Reforming

The steam reforming is an endothermic equilibrium reaction, in which hydrogen is obtained through a catalyzed reaction between a hydrocarbon and steam (1):

$$C_nH_m + n\ H_2O \leftrightarrows n\ CO + (n+1/2m)\ H_2 \quad (1)$$

Among the reforming processes, methane steam reforming (MSR) is the most feasible route to convert methane into hydrogen [13].

2.1.1. Methane Steam Reforming

Methane, with an energy density of 55.5 MJ·kg^{-1}, is the simplest hydrocarbon molecule; in reforming it is reacted with steam at 700–1000 °C under a pressure range of 3–25 bar [14]. In addition to carbon monoxide and hydrogen, in the gas stream at the outlet of the reformer, unreacted methane and carbon dioxide are also present, therefore, further treatment/purification steps are necessary for obtaining pure hydrogen. In particular, one [15] or two stages of CO-water gas shift [16,17] followed by selective methanation [18], preferential oxidation [19] or a treatment with permselective membranes [20]. Although noble metal-based catalysts provide high activity and good stability, the high cost and the limited availability of the noble metals prevent their use, so Ni/Al_2O_3 is the most used commercial catalyst for MSR [21]. Unfortunately, these catalysts suffer of serious deactivation, due to the coke formation and Ni particle sintering. It has recently been shown that the application of a uniform positive electric field is able to modify the catalytic behavior of Ni-based catalysts during methane steam reforming by improving the methane activation at the surface while reducing the coke formation [22]. Both experimental and computational observations suggested that the positive field promotes the oxidation of the Ni catalyst, through the activation of water at the catalyst surface, in addition, it suppresses the polymeric carbon formation. Increased performance can be obtained by the addition of promoters, such as cerium oxide [23], which is able to enhance the methane conversion and provide a beneficial effect on coke resistance as well. Sintering-resistant $Ni@SiO_2$ catalyst has been recently reported in which the encapsulation in thermally stable SiO_2 nanospheres, prevent the Ni nanoparticles migration and thus avoided aggregation [24].

One of the major challenges in MSR process, is the managing of the high reaction temperatures; to reach 700–800 °C at the center of the catalytic bed, 1200 °C on the external reactor wall are needed. The use of structured catalysts, obtained by coating highly conductive carriers, with the catalytic formulation, provide a flattening of radial thermal profile on the catalytic bed, thus lowering the outside temperatures [13]. Alternatively, it

has also been proposed to fill the voids of highly conductive open cell metal foams with small catalytic pellets, in order to exploit the radial heat transfer of the tubular reactor, due to the thermal conductivity of the interconnected solid matrix, while avoiding the washcoating of metal structures [25]. An inversion of the reactor configuration has been proposed, in which heat is provided from within the structure, so the reforming reaction is directly sustained by using the electrically driven SiC-based structured catalyst, obtained by washcoating a SiC heating element, without any external heat source [26]. Similar results have been obtained by using microwave heating for SiC-based structured catalysts, in which the dielectric properties of silicon carbide are used to transfer the heat directly to the catalyst, thus generating it directly inside the catalytic volume [27].

Intensification of the methane steam reforming process plays a key role, in order to achieve the objectives, set by the EU regulation. Indeed, electrification becomes competitive if the electricity used comes from renewable sources. The methane used in the reforming processes is mainly of fossil origin, however some studies have shown that the biomethane generated by the anaerobic digestion of sewage sludge can also be used [28]. A concrete alternative to methane comes from the use of biomass.

2.1.2. Bio-Oil Model Molecules Reforming

Concerning the thermal methods, two major routes to produce hydrogen from biomass are possible: the gasification to obtain syngas and the pyrolysis to obtain bio-oil, followed by reforming [29]. Bio-oil has larger energy density than biomass, composed by a mixture of organics including alcohols, carboxylic acids, aldehydes, ketones, furans, phenolics, etc. [30].

Several studies have recently been published in which the performance of bio-oil model molecules has been investigated. Comparative studies on the steam reforming of a series of organic molecules (methanol, formic acid, ethanol, acetic acid, acetaldehyde, acetone, furfural, guaiacol) derived from bio-oil, have demonstrated that the molecular structures drastically influence the reactivity and tendency to coking during steam reforming [29]. Methanol and formic acid could be reformed at low temperature, as they do not contain aliphatic carbons chain to be cracked, showing negligible coking (Figure 1). The steam reforming of ethanol, acetic acid, acetaldehyde, or acetone required much higher temperature, and generated remarkable amounts of coke deposits, especially acetone and acetaldehyde.

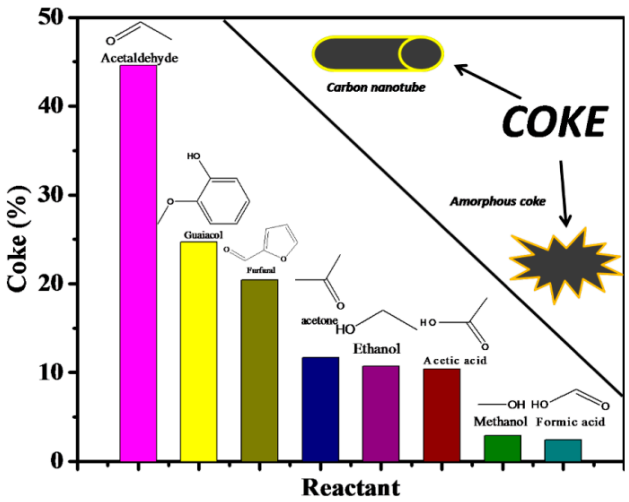

Figure 1. Coke formation trend per reactant molecule [29].

The characteristics of the catalyst play a fundamental role in the coke formation mechanisms. Comparative studies have showed that alumina support remarkably influences the catalytic stability of the catalyst, in methanol, acetic acid and acetone steam reforming [31].

The unsupported Cu showed lower stability than Cu/Al_2O_3, while the unsupported Ni showed higher stability than Ni/Al_2O_3, the unsupported Co was prone to coking.

In addition to the tendency to coke formation, a critical issue is the availability/renewability of the feedstock; bio-alcohols such as methanol, ethanol and glycerol can be easily obtained from renewable sources, therefore they seem to be a valuable alternative to natural gas.

2.1.3. Methanol Steam Reforming

Methanol can be obtained from biomass and CO_2, which makes it an attractive raw feedstock for reforming processes. The main advantage over ethanol is the lower tendency to coke formation, due to the high H/C ratio, moreover the absence of C-C bonds prevents the formation of a series of byproducts [32]. Cu-based catalysts are the most extensively studied catalysts for methanol steam reforming; although they show good activity at low temperature, the easily to sintering cause irreversible deactivation of the catalysts. To improve activity and stability of Cu-based catalytic systems, Cu-Al spinel oxide has been doped by adding MgO [33]. Mg^{2+} cations partially replaced Cu^{2+} incorporating into the spinel lattice, thus making it become hard to be reducible, consequently the doped catalysts showed a lower copper releasing rate and smaller copper particles. On the other hand, copper was successful used as promoter to increase the selectivity of Pd-based catalysts in methanol steam reforming [34]. The $CuPd/TiO_2$ bimetallic catalytic system showed improved performance, with respect the monometallic counterpart, by both thermo-photocatalytic and photocatalytic processes [35].

$CuFeO_2$-CeO_2 nanopowder catalyst, with a heterogeneous delafossite structure, prepared by the self-combustion glycine nitrate process, showed an improved H_2 generation rate of 2582.25 STP $cm^3 \cdot min^{-1} \cdot g_{cat}{}^{-1}$ at a flow rate of 30 sccm at 400 °C [36]. CuO/ZnO was successfully loaded onto a metal-organic framework material (Cu-BTC), thus improving the stability [37]. $(Ni_{0.2}Cu_{0.8})$/boron nitride nanohybrids have been studied, showing high catalytic stability and high CO_2 selectivity, moreover no carbon monoxide was detected during the full methanol conversion [38].

The effect of the support was also investigated in Cu/ZrAl-based catalysts, showing that the Zr/Al molar ratio of 0.4, in the support, improve the interaction between copper species and the support, resulting in a homogeneous distribution of highly dispersed Cu, with enhanced reducibility [39]. In a comparative study between different alumina supports, the commercial A520 MOF derived ɣ-Al_2O_3, in copper and palladium catalysts, has showed superior outcomes, attributed to the higher surface area, larger pore volume and possible defects in nanoscale alumina [40]. Different synthesis methods were also evaluated for CuZn/MCM-41 catalysts, revealing that the co-impregnation is the most effective method [41].

Alternative catalytic systems have been also proposed, for example $ZnCeZr_9Ox$ catalyst exhibited a full methanol conversion and an H_2 production rate of 0.31 $molh^{-1}g_{cat}{}^{-1}$ at 400 °C; the incorporation of Zn^{2+} into $CeZr_9Ox$ matrix, modulate the surface O_{Latt}/O_{Ads} ratio, and generate a Zn-O-Zr interfacial structure, corresponding to the lattice/bridge oxygen thus increasing the CO_2 selectivity [42]. Zn-modified Pt/MoC catalyst exhibited superior hydrogen production activity, with exceptionally low CO selectivity at low temperatures (120–200 °C), due to the formation of α-MoC_{1-x} phase and to the enhanced Pt dispersion [43]. In_xPd_y/In_2O_3 aerogels exhibited excellent CO_2 selectivity of 99% at 300 °C [44].

2.1.4. Ethanol Steam Reforming

Ethanol can be produced through fermentation of saccharides, and after distillation, bio-ethanol can be used in ethanol steam reforming (ESR); the post-ESR reformate has a high heating value of about 1450.9 $kJ \cdot mol^{-1}$ [45]. ESR has been investigated both by using simulated bio-ethanol feeding, and by using crude bio-ethanol or model mixture containing typical contaminants, however in the latter case, fast catalyst deactivation

occurs [32]. Nickel-based are the most studied catalysts for ESR, due to the low cost, as alternative cobalt and platinum have also extensively investigated. The major issue in ESR process is the carbon formation, different strategies have been proposed to overcome this limitation, such as the use of promoters and method to control the metal particle size.

Potassium has been successfully used as promoter of Co/Al_2O_3–CaO catalysts. The K-promoted catalysts showed higher hydrogen yield and lower methane selectivity than the unpromoted catalysts, mainly due to the suppression of methanation reaction [46]. On the other hands, sodium doping decreases the catalytic activity, but significantly increases the CO_2 selectivity, improving the H_2 selectivity, in $Pt/m\text{-}ZrO_2$ catalysts [47]. The addition of sodium favors the decarboxylation route, the decomposition of acetate at lower temperatures, yields methane and adsorbed carbonate, which decompose to carbon dioxide. Moreover, sodium promotes C-C scission. Ga doping of ceria-based catalysts improves the H_2/CO_2 ratio in ESR reaction, by changing the product distribution and reducing the coke formation [48]. The stability of Co/CeO_2 and Ni/CeO_2 catalysts have been improved by the La_2O_3 promoter, the carbon formation rate has been reduced as results of an increased active phase dispersion and a strengthening of the metal-support interactions [49].

In a comparative study, the effect of a series of promoters, including Na, Mg, Zr, La, Ce and the elements from K to Zn in the periodic table of elements, on Co/Al_2O_3 catalyst was evaluated [50]. Na, K, Cu, Ni and Ce addition promoted the catalytic activity, while Mg, Ca, Sc, Ti, V, Cr, Mn suppressed it, Na, K, Ca, Fe, Zn and La helped to suppress coking while Cu or Zr enhanced. Na suppressed the formation of acetyl species, while Cu promoted the acetyl species, C=O and C=C formation, bringing $Cu\text{-}Co/Al_2O_3$ towards coking.

A dragon fruit-like $Pt\text{-}Cu@mSiO_2$ catalyst for low temperature ESR reaction has been successfully synthesized by encapsulation strategy, with Pt-Cu alloy nanoparticles, of about 50 nm, embedded in the $mSiO_2$ [51]. This catalyst showed better performance than $Pt@mSiO_2$, $Cu@mSiO_2$ and the supported $Pt\text{-}Cu/mSiO_2$ catalysts, in terms of activity, H_2 selectivity, and stability. The mesoporous SiO_2 shell prevents leaching and aggregation of active sites and spatially suppresses the carbon deposition on the active surface (Figure 2).

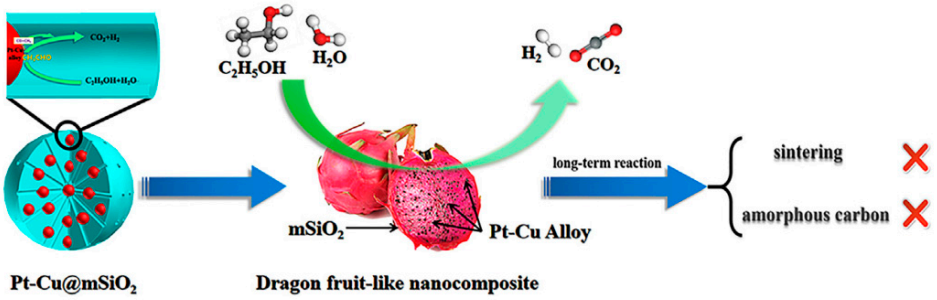

Figure 2. Schematic representation of the use in ESR of dragon fruit-like nanocomposite [51].

Graphene-encapsulated Ni nanoparticles (Ni@Gr), fabricated via in-situ growth method, showed good activity and durability in ESR at 550 °C [52]. Density functional theory calculations demonstrated that the presence of defects improved the adsorption energy of all reaction species. The primary reason for catalyst deactivation was the carbonaceous deposition. Spinel-type mixed manganese-chromium oxides $MnxCr_{3-x}O_4$, prepared by Pechini route have been used as support for the co-deposition of Ni and Ru; the strong metal-support interaction stabilized small clusters of metals/alloys, preventing carbon nucleation in ESR [53].

Biochar-supported Ni catalyst has also been used in ESR [54]. The results showed that biochar is a promising support as well as itself a reforming catalyst, in fact it contains alkali and alkaline earth metallic species and O-containing functional groups, which are factors affecting the catalytic performance.

2.1.5. Glycerol Steam Reforming

The use of glycerol in reforming processes is very promising; it can theoretically provide seven moles of hydrogen for every mole of $C_3H_8O_3$ [55], moreover glycerol is a by-product of biodiesel production, whose commercial value has been strongly affected by excessive supply. The use of glycerol for the production of value-added chemicals, such as hydrogen, appears to be the best way to exploit it and simultaneously increase the global biodiesel market [56]. Even in the case of glycerol steam reforming, the noble metal-based catalysts show excellent performance [57], in particular excellent activity has been found with Pt-based catalysts [55], moreover the presence of promoters suppresses the coke formation, however the high cost makes them uncompetitive compared to nickel-based catalysts [58].

The catalytic behavior of Ni catalyst supported on CaO-modified attapulgite in glycerol steam reforming, has shown that the addition of CaO promotes the dispersion of the active component, promoting the water gas shift reaction, thus leading to improved hydrogen yields [59]. Moreover, the addition of CaO enhances the inhibition of carbon deposition, prolonging the stability of the catalyst. The incorporation of CeO_2 into $NiAl_2O_4$ spinel is able to suppress the coke formation, through the formation of a $CeAlO_3$ phase which hinders the growth of filamentous carbon on nickel surface and enhances the gasification of carbon deposits by providing an oxidative environment around nickel active sites [60]. Recently, it has been showed that MgO is able to suppress the sintering of cobalt based catalysts in glycerol steam reforming, moreover the promotion with copper suppresses the coke formation [61].

The sintering of the active metal was suppressed in the bimetallic MNi/CNTs (M = Co, Cu and Fe, CNT = carbon nanotube) catalysts, in which Ni oxide was introduced into the cave and the other one was dispersed on the external wall of CNTs [62]. Flame spray pyrolysis has been successfully used to produce nano-sized Ni-based steam reforming catalysts for glycerol starting from $LaNiO_3$ and $CeNiO_3$ as base materials by varying the formulation, mixing them or incorporating varying amounts of ZrO_2 o SrO during synthesis [63]. The deactivation resistance was increased by improving the dispersion of nickel through the formation of Ni-La or Ni-Ce mixed oxide. ZrO_2 provided high thermal resistance, while a base promote /support, such as La_2O_3, downgraded the surface acidity of ZrO_2.

2.2. Autothermal Reforming

Autothermal reforming (ATR) is an interesting process which uses the heat of an exothermic reaction (partial oxidation, POX) to sustain the endothermic steam reforming reaction, by feeding air, steam, and the reacting feedstock, such as methane, methanol or ethanol to produce a H_2-rich stream. The main characteristic of ATR is the low energy requirements: by properly selecting the oxygen/fuel ratio, no external heat is required; moreover, oxygen availability may promote coke gasification reactions.

Ni-based catalysts are the most used in methane autothermal reaction, mainly due to the low cost; unfortunately, the sever reaction conditions can lead to the rapid deactivation of the catalyst. The use of promoters or bimetallic catalytic systems can improve the performance of these catalysts; series of 10Ni-M/$Ce_{0.5}Zr_{0.5}O_2/Al_2O_3$ catalysts (M = Pt, Pd, Re, Mo, Sn; molar ratio M/Ni = 0.003, 0.01, 0.03) have been tested in CH_4-ATR [64]. The catalysts with Pt, Pd, Re, or Mo, by contrast to the non-promoted sample, showed the ability to self-activate under the reaction conditions, making not necessary the catalyst pre-reduction, due to the improved reducibility. 10Ni-0.9Re/$Ce_{0.5}Zr_{0.5}O_2/Al_2O_3$ catalysts has shown high resistance to oxidation and sintering of the Ni active component as well as the resistance to coking.

The catalyst preparation method is one of the aspects that can improve the catalytic performance by enhancing the catalyst's physicochemical properties. These methods alter the metal-support interaction, thereby changing the kinetics of the catalyst which can result in enhanced productivity, reduced cost, and optimized energy requirements [65].

In a comparative study, bimetallic Cu-Ni catalysts, supported on binary oxides containing ZnO, ZrO_2, CeO_2 and Al_2O_3, were investigated, for the hydrogen production via the oxidative steam reforming of methanol [66]. At high temperature the most active catalyst was 30%Cu–10%Ni/$CeO_2Al_2O_3$, the good performance was attributed to the $Cu_{0.8}Ni_{0.2}$ alloy formation, as well as the high acidity and easy reducibility. At low temperatures, the best catalytic performance was obtained with 30%Cu–10%Ni/$ZrO_2Al_2O_3$. A series of CuO/$Ca_2Fe_2O_5$ catalysts, with different contents of copper were prepared as catalytic oxygen carrier (COC) which goes through the reduction → catalytic methanol conversion → re-oxidation route [67]. The results showed that the 40%Cu-loaded catalyst had the highest catalytic activity: the presence of $Ca_2Fe_2O_5$ tunes the redox activity and mobility of the lattice oxygen, obtaining a H_2 production rate of 37.6 $\mu mol \cdot H_2 \cdot g_{COC}{}^{-1} \cdot s^{-1}$ at 240 °C. Ni, Pt and a mixture of Ni and Pt supported on ZnO-rods were evaluated in methanol autothermal steam reforming, in the temperature range 200–500 °C [68]. The bimetallic catalysts showed the best catalytic activity, due to the formation of PtZn and NiZn alloys.

Pt-Ni/CeO_2-SiO_2 and Ru-Ni/CeO_2-SiO_2 catalysts were compared in an oxidative ethanol steam reforming reaction [69]. In both cases, the catalysts deactivated with time-on-stream, due to the severe reaction conditions; however, the Pt-based catalysts showed the highest ethanol conversion, hydrogen yield and the lowest carbon formation rate. A detailed kinetic mechanism has been also compared against experimental data and apparent kinetics, demonstrating that coke formation is associated with the 2-hydroxyethyl radical reaction path, explaining the effectiveness of the catalyst in coke suppression [70].

2.3. Gasification

Gasification is a process in which carbonaceous materials are converted in syngas, at high temperature, in presence of an oxidizing agent. Various types of biomass can be used as potential feedstocks for hydrogen production via gasification, including algae, food waste, municipal solid waste, and lignocellulosic biomass [71]. The hydrogen yield is strongly dependent on the process conditions of the biomass gasification, on the temperature of the steam flow but also on the type of raw material, which is a critical problem [72]. In a recent study, the optimization of biomass blending, which can be an effective way to overcome the problem of enormous feedstock variability, has been studied [73]. The simulation model used various biomass feedstock, including date pits, manure, and sewage sludge to correlate the biomass blending to the H_2/CO ratio in the obtained syngas, as alternative to the manipulation of process conditions.

One of the main problems of conventional gasification is the impossibility of using biomass with a high moisture content. Gasification in supercritical water (SCW) can directly use the biomass without drying process, since the reaction occurs in water phase. An experimental study on cornstalk gasification in SCW, carried out in the temperature range of 500–800 °C, a reaction time of 1–15 min and a feedstock concentration of 1–9%, has shown that the carbon gasification efficiency reaches 99% at the temperature of 700 °C, reaction time of 15 min and biomass concentration of 3% [74]. A parametric research on supercritical water gasification of food waste conducted with a micro quartz tube batch reactor (Figure 3), demonstrated that the complete gasification can be basically realized with a carbon gasification efficiency of 98% at a temperature of 850 °C, a concentration of 5 wt% and residence time of 10 min [75].

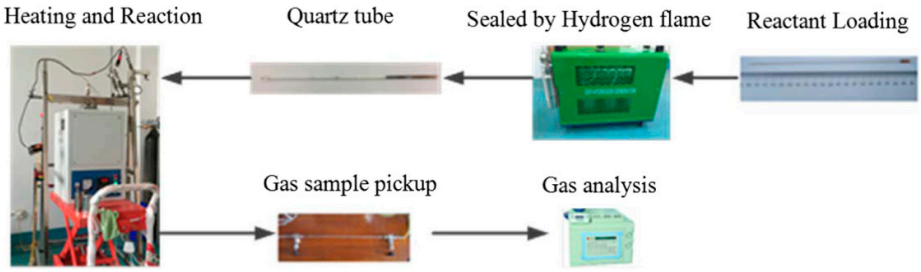

Figure 3. Supercritical water gasification experimental procedure with a micro quartz batch reactor [75].

2.4. Thermochemical Water Splitting

Water splitting is the reaction in which water is splitted into hydrogen and oxygen (2):

$$2\,H_2O + \text{heat} \rightarrow H_2 + O_2 \quad (2)$$

Complete decomposition in a single step can be obtained only at high temperatures (above 2000 °C), while thermochemical cycles, with multiple steps, and lower operating temperatures can supply the required heat [76]. The pure thermochemical cycles are driven either by only thermal energy (Figure 4a), while hybrid ones (Figure 4b) are driven by thermal and some other form of energy (e.g. electrical, photonic) [10].

In two-step thermochemical cycles, two separate reduction/oxidation steps utilizing a metal oxide as a reactive intermediate may be performed: (i) a higher valence metal oxide is reduced to the corresponding low valence metal oxide or metal and oxygen is produced (reduction step) and (ii) the lower valence metal oxide (or metal) reacts with water to form hydrogen and a higher-valence metal oxide (water splitting step), which is subsequently recycled in the first step [77]. The three-step processes can be obtained from the two-step one, in which the highest temperature reaction is replaced by a two-step reaction, thus achieving a reduction of the maximum temperature required. In most cases, the required temperature for water splitting decreases when more steps are employed, but the same decreasing trend also occurs for the efficiency potential due to the energy losses associated with heat transfer and products separation in each step. The sequence in the four-step cycles is: hydrolysis, evolution of hydrogen, evolution of oxygen and recycling of reagents [10].

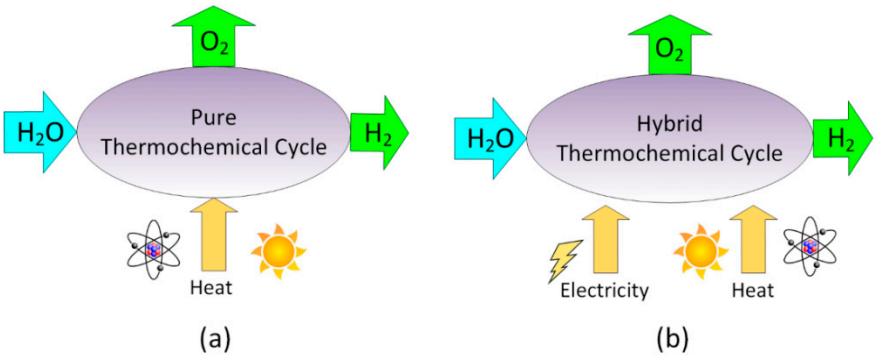

Figure 4. Schematic representation of pure (**a**) and hybrid (**b**) thermochemical cycles [10].

The four-step iron-chlorine (Fe-Cl) cycle was modelled by the Aspen Plus software package [78]. The results showed that the pressure does not significantly affect the reaction's production rates, while an increase in temperature favors oxygen production in reverse deacon reaction and magnetite production in hydrolysis and lowers hydrogen production in the hydrolysis step. Moreover, the steam/chlorine ratio is directly related to the HCl and oxygen production, in reverse deacon reaction and hydrogen production in hydrolysis.

Perovskite type mixed metal oxide compound, such as barium ferrite oxide, possesses good chemical and thermal stability under severe conditions, besides high oxygen storage capacity (OSC) and reducibility [79]. The addition of La^{3+} and Ga^{3+} to $BaFeO_{3-\delta}$ was investigated in water splitting, and the best performance was obtained with $Ba_{0.95}La_{0.05}FeO_{3-\delta}$, showing a H_2 production of about 1310 $\mu mol \cdot g^{-1}$ at 900 °C. Probably the smaller La^{3+} ionic radius compared to Ba^{2+} can lead to a larger lattice free volume for oxygen transport. The cubic perovskite $SrTi_{0.5}Mn_{0.5}O_{3-\delta}$ was tested in a water splitting cycle in which the material is thermally reduced at 1350 °C (pO_2, ~10−5 atm) and subsequently exposed to steam at 1100 °C (steam partial pressure of pH_2O = 0.4 atm), obtaining a hydrogen yield of 7.4 $cm^3 \cdot g^{-1}$ [80]. The cyclic operation did not show any degradation of the material, resulting in a constant 2: 1 yield of H_2/O_2.

$Ce_{0.9}Me_{0.1}O_y$ (Me = Fe, Co, Mn, and Zr) have been tested in thermochemical water splitting, both as powder and as mixed oxides reticulated porous ceramic (RPC) structures, obtained with sponge replica method [81]. The $Ce_{0.9}Fe_{0.1}O_y$ powder oxide showed the best hydrogen production (8.5 STP $cm^3 \cdot H_2 \cdot g_{material}{}^{-1} \cdot cycle^{-1}$) and stability during consecutive cycles, while the $Ce_{0.9}Fe_{0.1}O_y$ RPC sponge, showed an outstanding hydrogen production of 15 STP cm^3 $g_{material}{}^{-1} \cdot cycle^{-1}$ at a maximum temperature of 1300 °C, due to the to the open macroporosity of the reticulated porous ceramic structure, which enhanced both heat and mass transfer.

2.5. Remarks on Thermal Methods

The major drawback of thermochemical methods is the need to supply heat, which normally comes from fossil fuel combustion, typically by electric heating or by using a catalytic combustor [82]. To make these processes sustainable, not only must the feedstocks be renewable, but also the energy needed to the process should be sustainable too. For this reason, solar [83,84], wind and geothermal energy represent an interesting alternative to conventional methods, which, however, are feasible where cost savings are demonstrated. In a recent study a geothermal-assisted methanol reforming, incorporating a proton exchange membrane fuel cell, for hydrogen production, has been proposed [85]. Thermodynamic and economic assessment have showed that an annual cost-saving can be obtained of 20.9%, compared with the conventional system. Another issue is the significant production of CO_2 as byproduct, which can be captured by sorbents, such as CaO in the sorption enhanced steam reforming processes, thus improving the H_2 yield [86]. Membrane-assisted steam reforming is also an intriguing option for H_2 production from biomass, especially in refueling stations for automotive fuel cells [87]. The energy consumption required for H_2 compression can be significantly reduced if the process supplies H_2 at high pressures. Thermodynamic analyzes show that, in the case of ESR, reforming temperatures above 550 °C are required to obtain H_2 partial pressures that will allow operation without sweep gas, obtaining appreciable energy savings. Thermochemical water splitting presents some significance advantages, including no need of electricity in pure water splitting and no need of membranes for the hydrogen separation [10]. Biowaste-based biomethane as a feedstock for hydrogen production, in reforming processes, seems to be an intriguing option, as it can lead to negative life-cycle greenhouse gas emissions even without CO_2 capture and storage (CCS) [88]. Reforming-based hydrogen production processes with CCS can be considered a clean technology, as the life-cycle greenhouse gas emissions are lower than those of hydrogen from electrolysis, considering that the most of electricity supplied, is still largely based on fossil fuels [88].

3. Photocatalytic Methods

In the framework of photocatalytic methods, we basically refer to hydrogen production by water splitting using solar energy, through the generation of electron-hole pairs by photons and semiconductors [89].

Photoexcited electron-hole pairs can be separated efficiently using sacrificial agents, which allow the formation of hydrogen with reduced electron-hole pair recombination.

Nowadays, however, this process faces challenges in being implemented using visible light, given its low photon conversion efficiency [89]. To achieve photocatalytic water splitting, feasible photocatalysts must meet some fundamental criteria: they must absorb visible light (display suitable band gaps), they must be chemically stable under redox conditions, they must have a low cost, they must be recyclable, they must be chemically resistant and they must be adaptable for large-scale hydrogen production. In this sense, the design of efficient photocatalysts with high photo-conversion efficiency is the target for completing the photocatalytic hydrogen evolution [89].

In the last years different configurations have been proposed, including CuS- and NiS-based heterojunctions, titanium dioxide based core–shell structures and periodical structures with excellent adsorption ability, and imogolite hollow cylinders [90], as well as S-scheme heterostructure [91]. Among them, the titanium dioxide based ones are the most interesting, due to the chemical resistance properties, accessibility, and affordability [92]. Moreover, in recent years the scarce activation of titanium dioxide by visible sunlight has been mitigated; novel strategies of doping development of novel composites are allowing to obtain interesting results also in the field of visible light-activated photocatalysis [92]. The addition of different metals to titanium dioxide results in increasing the hydrogen production under visible light. In the case of palladium [93], a "series-parallel" reaction network has been proposed for describing the water splitting reaction using the mesoporous Pd-TiO_2 and ethanol as organic scavenger (Figure 5) [94].

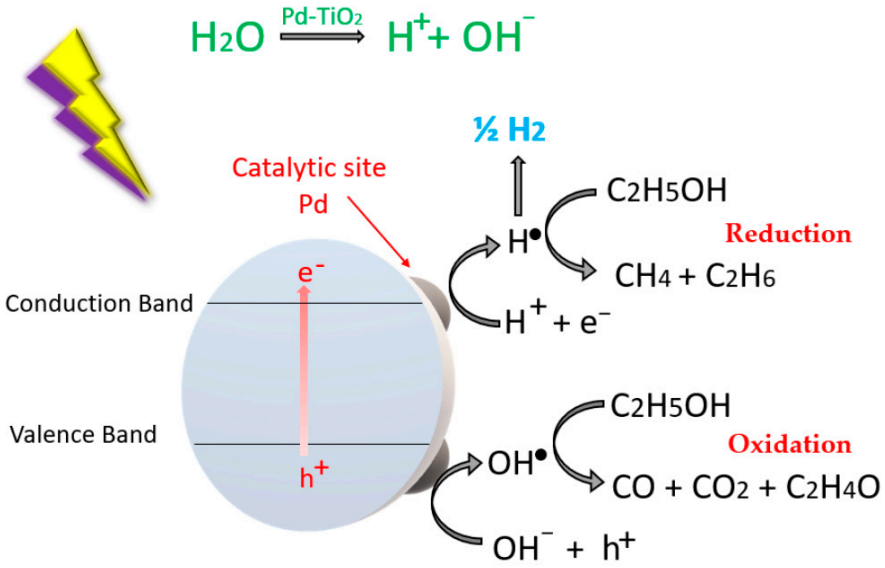

Figure 5. Schematic illustration of the three water splitting methods [94].

The addition of earth-abundant metals has a positive effect, in particular in the case of Ni [95] and Cu [96,97]. A high activity in hydrogen evolution under visible light has been demonstrated also for solid solutions of cadmium and manganese sulfides, due to their valence and conduction band position tuning, and for composite photocatalysts, CdS-β-Mn_3O_4-MnOOH, due to the ternary heterojunction formation [98]. Although reasonable research progress has been accomplished on the design of photocatalysts with high-conversion efficiency, there are still some issues to be addressed. For example, most metal chalcogenides-based heterojunctions can only split water in the presence of sacrificial agents.

Photocatalysis may also be used for hydrogen production from water, by using titania-containing gold nanoparticles [99], or wastewater pollutant removal, by using TiO_2-based catalysts [100,101] or metal halide perovskites [102]. In the latter processes, the contemporary targets of hydrogen production and the abatement of harmful pollutants may be reached, with an evident environmental benefit.

Hydrogen production may also be obtained through the so called "photoreforming processes" of organic substrates, such as methanol, ethanol, glycerol, sucrose, glucose, starch and wood [103], as well as of aromatic water pollutants [104]. In these processes, modified TiO_2-based catalysts are the most used materials for having higher hydrogen evolution.

The main problems of catalytic water splitting are the need for sacrificial reagents, typically organic, whose cost and environmental impact is not negligible, the development of more active visible light photocalysts and the design of low-cost reactors. These problems make these methods uncompetitive from an economic point of view.

4. Biological and Photonic Methods

Biological processes allow producing hydrogen from renewable resources such as biomass and solar energy; the main processes can be classified as direct/indirect photolysis, photo-fermentation, dark-fermentation, and CO gas-fermentation [105].

4.1. Dark-Fermentation

In dark-fermentation process, hydrogen is produced from organic materials, such as sugars, amino acids, waste materials, wastewaters and so on, without light, by using anaerobic organisms [106]. Dark-fermentation is considered a promising alternative to traditional hydrogen production methods, due to the low estimated production costs [107]. Hydrogen-producing bacteria can be classified as spore-forming obligate anaerobic bacteria, non-sporulating anaerobes and, facultative bacteria (Figure 6) [108]. The *Clostridium* bacteria, belonging the spore-forming obligate anaerobic microorganisms, are considered the most efficient bacteria in hydrogen production; the fermentation can be both acetate-type (3) and butyrate-type (4) [108].

$$C_6H_{12}O_6 + 2H_2O \rightarrow 2CH_3COOH + 4H_2 + 2CO_2\ \Delta G^\circ = -206\ kJ{\cdot}mol^{-1} \quad (3)$$

$$C_6H_{12}O_6 \rightarrow CH_3CH_2CH_2COOH + 2H_2 + 2CO_2\ \Delta G^\circ = -255\ kJ{\cdot}mol^{-1} \quad (4)$$

The yield of the process depends on a series of factors: pH, temperature, pressure, the hydraulic retention time [109], the type of organism, the composition of the substrate and the presence of metals, and several studies focus on the effects of changing these parameters. For example, the dark-fermentation can take place both with indigenous bacteria and by adding microbial inoculum; a recent study focused on determining if the indigenous bacteria associated with thermal pretreatment can impact on the performance [110]. The study has been carried out on seven organic substrates and has demonstrated that the indigenous bacteria are effective as the thermally pretreated exogenous bacteria in producing hydrogen. The highest hydrogen yield was obtained with Clostridiales and Enterobacteriales.

The invasive aquatic weed *A. philoxeroides* has been used to evaluate the effect of a steam-heated acid pretreatment and enzymolysis on the dark-fermentation, by using *Enterobacter aerogenes* ZJU1 mutagenized by ^{60}Co-γ irradiation as inoculum [111]. The study showed that the acid treatment significantly disrupts the fiber of the *A. philoxeroides*, contributing to the higher yield in reducing sugar and consequently a hydrogen yield increase by 59.9%. The effect of salinity and pH on dark-fermentation of swine wastewater pretreated with thermophilic bacteria, has showed that 1.5% of salinity and a pH = 6 are the optimal condition for hydrogen production, while 3.5% of salinity and pH = 5 are able to inhibit the production [112].

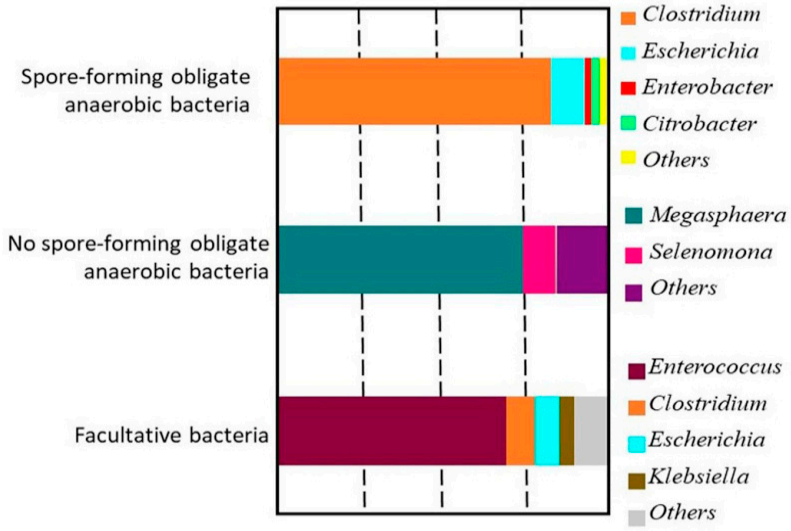

Figure 6. Three examples of the taxonomic composition of H_2-producing communities dominated by the different groups of H_2-producing microorganisms [108].

The use of lawsone and anthraquinone 2-sulphonate covalently immobilized on activated carbon, as redox mediators, has been evaluated in the dark fermentation of glucose by a pretreated anaerobic sludge [113]. The results showed that the use of lawsone increased the hydrogen production of 10%, while anthraquinone 2-sulphonate improved the hydrogen production rate of 11.4%. A remarkable increase in hydrogen production from waste activated sludge was obtained by freezing in the presence of nitrite [114]. The pretreatment accelerates the disintegration of sludge and promote the biodegradable organics released, thus providing more bio-available substrate for hydrogen production.

The iron hydroxide mineral ferrihydrite is able to promote the hydrogen production by Clostridium, redirecting the metabolic pathways and stimulating the bacterial growth, thus improving the carbon and electron conversion [115]. The addition of iron and nickel nanoparticles improve the fermentation process enhancing the hydrogen production by *Clostridium butyricum* [116]. Similar improvements were obtained by including NiO and CoO nanoparticles to dark fermentation of rice mill wastewater using *Clostridium beijerinckii* DSM 791 [117].

One of the main problems, related to this process is the homoacetogenesis (5) [108]:

$$4H_2 + 2CO_2 \rightarrow CH_3COOH + 2H_2O\ \Delta G^\circ = -104\ kJ \cdot mol^{-1} \quad (5)$$

Due to the negative impact on the hydrogen production, prevention, and control of homoacetogenesis are being studied. Currently there is no method to completely eliminate homoacetogenic bacteria, as their presence depends on the culture, substrate and process parameters. The strategy to minimize its impact is therefore to control CO_2 and H_2 concentrations during the process. For example, studies on the effect of shear velocity on hydrogen production, in a dynamic membrane bioreactor, containing a 50 μm polyester mesh as support material, have shown that the homoacetogenic pathway can minimized by choosing the optimal shear velocity, thus improving the hydrogen production [118].

4.2. Photofermentation

Photofermentation is a process in which hydrogen is produced from organic compounds through a nitrogenase-catalyzed reaction, in the presence of light energy, by photosynthetic or anaerobic bacteria, such as *Rhodobium*, *Rhodobacter*, *Rhodospirillum*, and Rho*dopseudomonas* [119]. The major limitations to the industrialization of photofermenta-

tion are the availability and distribution of light and to the need for specific substrates, i.e., small fatty acids, including acetate, propionate and butyrate [120]:

$$CH_3COOH + 2H_2O + Light \rightarrow 4H_2 + 2CO_2 \qquad \Delta G^\circ = +104\ kJ \cdot mol^{-1} \tag{6}$$

As in the case of dark-fermentation the influence of a series of process parameters have been recently studied, with the aim of optimizing the hydrogen production from photo-fermentation.

Lighting and mixing significantly affect the hydrogen production performance from agricultural waste (Figure 7); mixing enhance the mass transfer and shorten the lag phase, however the higher is the mixing speed the higher is the light intensity requirement [121]. Intermittent stirring has shown to increase the hydrogen production rate of 65.05% compared to continuous stirring, in corn stover hydrolysate photo-fermentation [122].

A combination of ultra-sonication and biosorption using banana peels waste pretreatment, for mixed effluents of 70% restaurant and 30% brewery, enhance the photo fermentative hydrogen production processes [123]. Addition of glycerol to *Arundo donax* L. can enhance the hydrogen production via photofermentation, due to redox potential [124]. The highest hydrogen yield (79.2 $cm^3 \cdot g_{substrate}{}^{-1}$) was obtained with a glycerol: *Arundo donax* L. ratio 1:1.

Substrate concentration has been shown to be crucial in the process of photo-fermentation hydrogen production in a study using potato taken as a starch-rich agricultural leftover under fluctuating conditions [125].

The effects of NaOH and $Ca(OH)_2$ pretreatments on giant reed for the photofermentative hydrogen production, was evaluated [126]. The results showed that the 20% NaOH pretreated giant reed biomass reached the highest hydrogen yield (98.3 $cm^3 \cdot g_{TS}{}^{-1}$; TS = total solids), which was 20% and 70% higher than the highest level obtained with Ca $(OH)_2$ pretreated (20% $Ca(OH)_2$) and untreated giant reed, respectively. The optimal substrate concentration of 25 $g \cdot dm^{-3}$ was found beneficial to hydrogen production, in cellulase and protease hydrolysis of *Chlorella* biomass [127].

The effect of enzymolysis time on the hydrogen production by photofermentation of energy grasses was also studied [128]. The results showed that the hydrogen production rate was depending on the kind of grass, however the highest hydrogen yield was obtained from *Medicago sativa* L. with an enzymolysis time of 60 h (147.64 $cm^3 \cdot g_{TS}{}^{-1}$), the highest hydrogen production rate was obtained from *Arundo donax* with an enzymolysis time of 36 h (5.53 $cm^3 \cdot h^{-1} \cdot g_{TS}{}^{-1}$) obtained, while the highest hydrogen production efficiency was obtained from *Miscanthus* with an enzymolysis time of 0 h (1.15 $cm^3 \cdot h^{-1} \cdot g_{TS}{}^{-1}$).

Hydrogen production is strongly dependent on the pH and inoculation volume ratio [129]; it is well known that a decrease in pH, due to metabolic acid production, is a limiting factor in hydrogen production during the photofermentation from glucose [130].

A buffer solution Na_2HPO_4/NaH_2PO_4 has shown to be able to improve the buffer capacity of fermentation broth, thus improving the hydrogen production by photo-fermentation from corn stalk [131]. The highest energy conversion efficiency 9.84%, hydrogen yield 132.69 $cm^3 \cdot g^{-1}$ of corn stalk, and hydrogen content 53.88% were achieved at pH value of 6. The initial pH value of phosphate buffer has a crucial role on the hydrogen production, in fact with the increase in pH values, the hydrogen production gradually delays, suggesting that the alkaline environment has a negative effect on the ability of photosynthetic bacteria [132]. A pH equal to 7 was found to be the optimal value for the hydrogen production from potato residue [133].

Response surface methodology was used to study the dependence of initial pH, substrate concentration, and cellulase loading on photo-fermentation hydrogen production by HAU-M1 from alfalfa, and to find the optimal conditions [134]. The highest hydrogen production yield of 55.81 $cm^3 \cdot g^{-1}$ was observed at initial pH of 6.90, substrate concentration of 31.23 $g \cdot cm^{-3}$, and cellulase loading of 0.13 $g \cdot g^{-1}$.

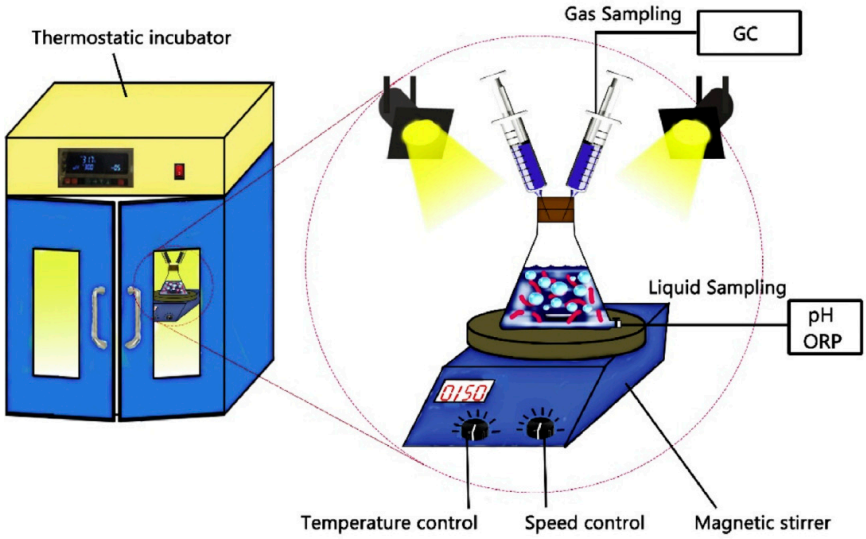

Figure 7. Diagram of photofermentation hydrogen production [122].

A study on the effect of different pretreatments, such as hydrothermal, acid, alkali, acid-heat, and alkali-heat on the structural characteristics, enzymatic saccharification and photo-fermentation of corn straw, has shown that all the treatments effectively destroyed the corn straw structure and improved its enzymatic saccharification potential [135]. The highest cumulative hydrogen yield (137.76 $cm^3 \cdot g_{TS}^{-1}$) was obtained with the 2% NaOH pretreated corn straw, while the minimum (44.20 $cm^3 \cdot g_{TS}^{-1}$) was obtained with a pretreatment of 4% NaOH-heat.

The addition of iron, molybdenum, and EDTA to the photofermentation of a blend of pre-treated brewery (30%) and restaurant (70%) effluents, was found beneficial for the hydrogen production and bacterial growth by *Rhodobacter sphaeroides* 158 DSM [136]. The additions of Fe at 70 µM, Mo at 14 µM, and co-addition of Fe:Mo at 70 µM:8 µM to the mixture increased the cumulative biohydrogen production of 69%, 27% and 160 93% respectively. The addition of EDTA was able to further increase the hydrogen production, but it is crucial to choose an optimal concentration in order to avoid chelating effects.

To make the process more competitive, the production of interesting chemicals, in addition to hydrogen, can be considered. For example, hydrogen and poly-β-hydroxybutyrate can be contemporary obtained by single-stage photo-fermentation of winery wastewater, by using a purple non-sulfur bacteria mixed consortium [137]. With an initial chemical oxygen demand of 1500 $mg \cdot dm^{-3}$, up to 468 $cm^3 \cdot dm^{-3}$ of hydrogen and 203 $cm^3 \cdot dm^{-3}$ of poly-β-hydroxybutyrate can be produced.

4.3. CO Gas-Fermentation

In CO gas-fermentation hydrogen is produced by reacting carbon monoxide and water in presence of photosynthetic bacteria under anaerobic conditions, through the overall reaction (7) [105]:

$$CO + H_2O = CO_2 + H_2 \ \Delta G^\circ = -201 \ kJ \cdot mol^{-1} \quad (7)$$

Although this technique is promising for hydrogen production, hydrogen consumption by homoacetogenesis still remains the main challenge. In a recent study, the effect of pH and CO loading, on the CO and carbohydrate-rich wastewater co-fermentation was investigated, focusing on the homoacetogenesis behavior [138]. The results showed that the highest hydrogen production was obtained with at pH = 5 with a CO loading of 2000 $cm^3 \cdot d^{-1}$; the hydrogen consumption increased with the pH from 5 to 8, moreover the injection of CO further increased the hydrogen consumption at neutrophil pH = 7–8. In an interesting study, the possibility to produce both thermophilic enzymes and hydrogen at the same time has been demonstrated, by using hyperthermophilic strain Thermococcus

onnurineus NA1 156T for CO fermentation, providing the basis for cell factories to upcycle industrial waste gas [139].

4.4. Bio-Photolysis

Bio-photolysis can be defined as a "photonic-driven hydrogen production" process, in which water splitting is obtained by using cyanobacteria and blue-green algae [119]. It is categorized in direct bio-photolysis and indirect bio-photolysis (Figure 8). The direct route consists of a photosynthetic reaction and uses microalgae in presence of solar energy (8) [140]:

$$2H_2O + \text{Light energy} \rightarrow O_2 + 2H_2 \quad (8)$$

The indirect bio-photolysis is a two-step process, the first step is the photosynthesis (9) while the second step hydrogen and CO_2 are generated (10) [140]:

$$12H_2O + 6CO_2 + \text{Solar energy} \rightarrow 6O_2 + C_6H_{12}O_6 \quad (9)$$

$$C_6H_{12}O_6 + 12H_2O + \text{Solar energy} \rightarrow 6CO_2 + 12H_2 \quad (10)$$

Hydrogen is produced by hydrogenase and nitrogenase enzymes.

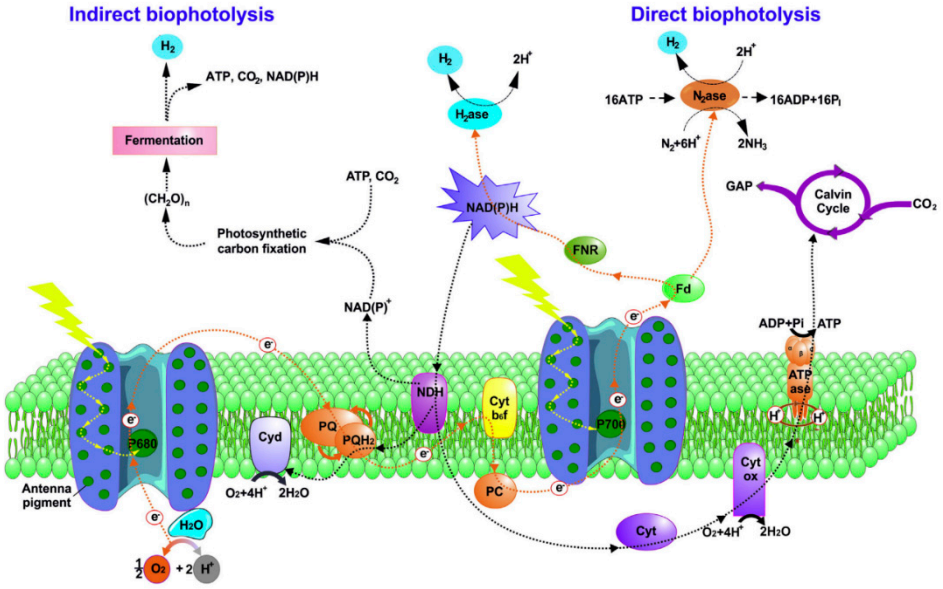

Figure 8. Direct and indirect biophotolysis processes of photosynthetic microorganisms Abbreviation: Cyd, cytochrome bd quinol oxidase; PQH_2/PQ, plastoquinol/plastoquinone; ATPase, ATP synthase; Cyt b_6f, cytochrome b_6f complex; Fd, ferredoxin; FNR, ferredoxin NAD(P) reductase; H_2ase, hydrogenase; NDH, NAD(P)H dehydrogenase; PC, plastocyanin; PQ, plastoquinones; P680, Photosystem II; P700, Photosystem I; N_2ase, nitrogenase; H_2, hydrogen [141].

The hydrogen yield was evaluated in a comparative study with four cyanobacteria strains (*Synechocystis* sp. PCC 6803, *Desertifilum* sp. IPPAS B-1220, *Synechococcus* sp. I12, and *Phormidium corium* B-26) [141]. The maximum hydrogen accumulation was obtained with the wild-type, filamentous, non-heterocystous cyanobacterium *Desertifilum* sp. IPPAS B-1220. The yield was 0.229 $mmol \cdot mg_{chlorophyll}{}^{-1} \cdot h^{-1}$ in the gas phase within 166 h in the light, which, based on the data reported by the authors in the article, is among the highest one reported in the literature, for these cyanobacteria.

4.5. Integrated Systems

The critical aspect of biological processes is certainly the low yield to hydrogen, especially due to the presence of byproducts. One strategy for increasing efficiency lies in combining multiple processes. For example, a process has been reported in which

duckweed are used as feedstock for hydrogen production, through dark fermentation, simultaneously using the fermentative waste to produce microalgal lipids [142]. The simultaneous production of hydrogen and the use of waste reduce the costs of microalgae cultivation and wastewater treatment. More attention has received the sequential two-stage dark and photo-fermentation process. The volatile fatty acids produced during the dark-fermentation are used for the hydrogen production in photo-fermentation. Combining the two processes is possible to greatly improve the hydrogen production; as obvious from the previous overall reactions (3) and (6), in the acetate-type fermentation four moles of hydrogen and two moles of acetic acid are obtained from one mole of glucose, subsequently the two moles of acetic acid give eight moles of hydrogen [143]. Some articles, focusing on this double-stage process, have been published in the last year [144]. The dark-fermentation effluents, with low-butyrate and high lactate concentration, were used to maximize the hydrogen yield in photo-fermentation process, using fruit and vegetable waste and cheese whey powder [145]. The strategy was optimizing the C/N ratio to take advantage from higher hydrogen yield obtainable with lactate in photo-fermentation. L-cysteine and Fe_3O_4 nanoparticles can improve the hydrogen production and the electronic distribution from dark-fermentation effluents in photo-fermentation, by acting as reducing agent and by enhancing the bacteria aggregation [146]. Improved hydrogen production was also obtained by adding Fe(II) sulfate concentration during photo-fermentation stage [147]. The addition of enzymatic hydrolysate is able to increase the H_2 yield from 312.54 to 1287.06 $cm^3 \cdot H_2 \cdot g_{TOC}{}^{-1}$ (TOC = total organic carbon), and maximum hydrogen production rate from 2.14 to 10.23 $cm^3 \cdot h^{-1}$, in the photo fermentation from dark fermentation effluents [148]. The efficiency of organic waste conversion to hydrogen was enhanced through the addition of Ca- and Mg-saturated resin and phosphate-laden biochar in a single-stage hybrid dark-photo hydrogen fermentation from food waste [149]. The saturated resins provided the nutrients for the bacteria, by gradual releasing calcium and magnesium, while biochar promoted bacterial adhesive growth and acted as a buffer, due to the presence of phosphate, amino, and carbonate compounds.

To investigate a sequential dark and photofermentation process for the treatment of wastewater and the simultaneous hydrogen production, a circular baffled reactor (Figure 9), operating at ambient temperature was introduced [150]. The highest hydrogen yield (0.4 $dm^3 \cdot g_{COD}{}^{-1}$), a chemical oxygen demand (COD) removal of 82%, and an organic-N removal of 95% were obtained at the hydraulic retention time of 24 h and at the initial pH of 6.5. The techno-economic evaluation highlighted the feasibility when dealing with gelatin-rich wastewater.

Simultaneous hydrogen and poly-β-hydroxybutyrate-PHB productions, under dark, photo, and subsequent dark and photofermentation, by using wastes, has been reported [151]. In the sequential dark and photofermentation the highest hydrogen and PHB were obtained by using rice straw hydrolysate (1.82 ± 0.01 $mol_{H2} \cdot mol_{glucose}{}^{-1}$ and 19.15 ± 0.25 $g \cdot dm_{PHB}{}^{-3}$) at a pH of 7.0, with *Bacillus cereus* (KR809374) and *Rhodopseudomonas rutile*.

In a comparative study, batch, semi-continuous and continuous mode for hydrogen production from dark fermentation effluents were investigated. The results highlighted the best performance of the semi-continuous mode [152].

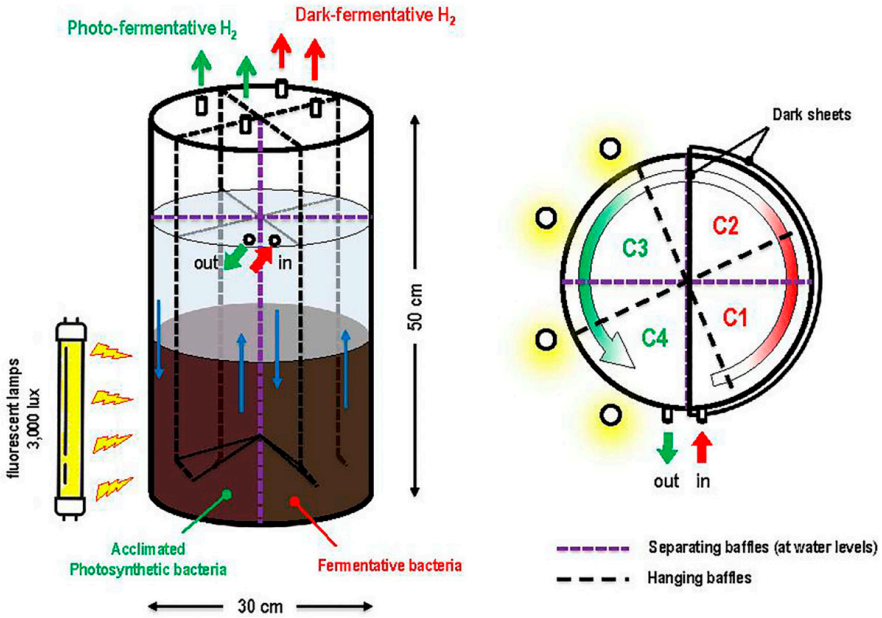

Figure 9. Schematic diagram for the lab-scale dark-photo circular baffled reactor used for anaerobic treatment of gelatinaceous wastewater [150].

4.6. Comparative Studies

Comparative studies among photofermentation, dark fermentation and dark-photo co-fermentation methods, by using photosynthetic HAU-M1 bacteria and dark fermentative *Enterobacter aerogenes* bacteria, have demonstrated that photofermentation is the most promising method for hydrogen production from corn stover, due to its maximum cumulative hydrogen yield of 141.42 $cm^3 \cdot g_{TS}^{-1}$, maximum hydrogen production rate of 6.21 $cm^3 \cdot g_{TS}^{-1} \cdot h^{-1}$, maximum hydrogen content of 58.90% and highest energy conversion efficiency of 10.12% [153]. Pretreatment by alkaline-enzymolysis has successfully been used also with cornstalk hydrolysate (CS), to improve the hydrogen yield [154]. The maximum hydrogen yields of 168.9 $cm^3 \cdot g_{CS}^{-1}$, 357.6 $cm^3 \cdot g_{CS}^{-1}$, and 424.3 $cm^3 \cdot g_{CS}^{-1}$ were obtained in dark fermentation, photofermentation, and two-stage fermentation, respectively, with $Ca(OH)_2$ 0.5%, hydrolysis temperature 115 °C, hydrolysis time 1.5 h, cellulase dosage 4000 $U \cdot g_{CS}^{-1}$ and xylanase 4000 $U \cdot g_{CS}^{-1}$.

4.7. Remarks on Biological and Photonic Methods

Among the biological methods, the most cost-effective process is dark fermentation [143], due to low production and capital cost and good hydrogen yield. However, if compared with other production methods, the hydrogen yield and production rate are still uncompetitive and the production processes are still at a primordial stage, moreover another critical issue is the availability and pre-treatment of inocula [155]. The design of integrated systems can reduce costs and increase the hydrogen production; the sequential two-stage dark and photo-fermentation process, using wastes as feedstock, seems to significantly improve the hydrogen production, however at the moment this type of technology seems more suitable for small plants, for the local production of hydrogen.

5. Electrical Methods

In the framework of the electrical methods, we basically refer to the water electrolysis, in which hydrogen and oxygen are produced from a molecule of water (11):

$$\text{Overall reaction:} \qquad 2\,H_2O \rightarrow 2\,H_2 + O_2 \tag{11}$$

Unfortunately, the water dissociation requires a significant amount of energy (ΔH^0 = 285.8 $kJ \cdot mol^{-1}$ and ΔG^0 = 237.2 $kJ \cdot mol^{-1}$ under standard conditions); therefore,

the cell voltage required for water dissociation is 1.23 V under standard conditions [156]. The main limitation of the process is the slow kinetics, to reach a significant hydrogen production rate, cell voltages of 1.8–2.0 V are required, thus increasing the costs, and decreasing the efficiency of the process [156]. There are several water electrolyzes technologies, however the major types of cells commercially available are: alkaline electrolysis cell (AEC), anion exchange membrane electrolysis cell (AEMEC) proton exchange membrane electrolysis cell (PEMEC), and solid oxide electrolysis cells (SOEC) [157].

5.1. Alkaline Electrolysis Cell

In alkaline electrolysis cell, the electrodes are immersed in the liquid electrolyte, typically a 25–30 wt% solution of KOH or NaOH separated by a diaphragm. Anodic (12) and cathodic reactions (13) are the following:

$$\text{Anodic reaction:} \quad 4\,OH^- \rightarrow O_2 + 2H_2O + 4\,e^- \tag{12}$$

$$\text{Cathodic reaction:} \quad 2\,H_2O + 2\,e^- \rightarrow H_2 + 2\,OH^- \tag{13}$$

The choice of the electrocatalysts is a critical issue, those based on noble metals are highly efficient, on the other hand, the most convenient material used for the electrodes are Ni-based [158,159], however to improve the performance and reduce the degradation, a series of metals can be used as additives, including cobalt, vanadium iron and selenide [160]. The use of noble metal-based electrodes could provide better performance however, cheaper alternative would be preferred. Recently MoO_2-Ni arrays have been reported to exhibit a Pt-like activity at 25.0 °C [161], its heterogeneous components may avoid agglomeration under high-temperature catalytic conditions.

High efficiency is obtained when the cells operated at low current densities (<0.4 $A{\cdot}cm^{-2}$). Historically the most common diaphragm is of porous white asbestos ($Mg_3Si_2O_5(OH)_4$). Due to the toxicity problems related to the use of asbestos, in the last decade considerable efforts have been put into developing hydroxide conducting polymers suitable for alkaline water electrolysis [159].

The chance of using higher current density collides with the gas bubble generation, trapped in porous electrodes, resulting in the reduced accessibility to the active sites. Recently 3D printed electrodes, with a controlled periodic structure, have been reported, which are able to suppress the gas bubble coalescence, jamming and trapping [162]. The 3D-electrodes decorated with carbon-doped NiO can reach a current density of 1000 $mA{\cdot}cm^{-2}$ in a 1.0 M KOH electrolyte at hydrogen evolution reaction and oxygen evolution reaction overpotentials of 245 and 425 mV, respectively. In a comparative study, the tradeoff between surface area and pore structure, in nickel electrodes—foam, microfiber felt, and nanowire felt—has been studied [163]. The results showed that the microfiber felt is able to maintain a current density of 25 000 $mA{\cdot}cm^{-2}$ over 100 h without degradation, balancing high surface area with the ability to remove bubbles.

5.2. Anion Exchange Membrane Electrolysis Cell

Unlike the AEC, in the case of anion exchange electrolysis cell, the hydroxyl anions cross a membrane. Typically, metal transition oxides electrocatalysts are used at the anode, and rare-earth metal oxides are used at the cathode [156]. Recently nanostructured nickel-based electrode films have developed, prepared by magnetron sputtering, in an oblique angle configuration, showing good performance [164]. $NiMn_2O_4$ anode catalyst was developed and tested in combination with a commercial FAA3-50 membrane, a durability test was carried out for 1000 h by varying the cell potential between 1 and 1.8 V for the FAA3-50 and $NiMn_2O_4$ based-MEA, showing high stability [165].

Much effort has been focused on the development of highly efficient membranes. Twisted ether-free polyarylene piperidinium, synthesized via acid-catalyzed polycondensation reaction, characterized by efficient ion-conducting channels, which provide an hydroxide conductivity of 37 $mS{\cdot}cm^{-1}$ at 30 °C, has been proposed [166]. The cell based

on this membrane has a high current density of 1064 mA·cm^{-2} at 2.5 V under 1 M KOH and 50 °C and a high frequency resistance of 0.165 Ω·cm^{-2} at 1.8 V. The durability test, performed at current density of 200 mA·cm^{-2} showed a voltage of 2.1 V for more than 500 h.

The effects of ion-exchange capacity and thickness of all-hydrocarbon anion exchange membranes was investigated [167]. The best performance was obtained by using a membrane with a ion-exchange capacity of 2.1–2.5 meq$_{OH^-}$g^{-1} and a thickness of 50 µm, and the FAA-3 ionomer in a 1 M KOH liquid electrolyte at 60 °C. Under these conditions, a potential of 1.82 V was obtained at a current density of 2 A·cm^{-2} and a cell resistance of 95 mΩ·cm^2.

In a comparative study, the performance of Sustanion®, Aemion™ and A-201 membranes were investigated [168]. Good performance at temperatures up to 60 °C, at KOH concentrations of 0.5–1 M were obtained in all the cases, the use of distilled water led to an increase in the membrane resistance, while the best performance was obtained with the Sustanion®-based membrane electrode assembly (MEA, Figure 10) at all KOH concentrations and temperatures studied.

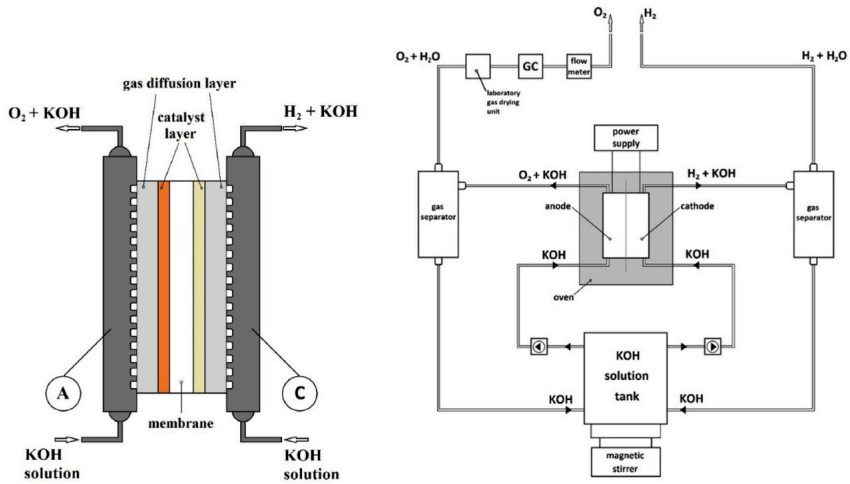

Figure 10. Scheme of the zero-gap cell (left) and the electrolysis cell testing bench [168].

5.3. Proton Exchange Membrane Electrolysis Cell

In the proton exchange electrolysis cell, the anodic and the cathodic compartments are separated by a polymer membrane. In the anodic compartment, water is oxidized according to the reaction (14); the hydrated protons migrate across the membrane to reach the cathode where they are reduced (15):

$$\text{Anodic reaction:} \qquad 2\,H_2O \rightarrow O_2 + 4\,H^+ + 4\,e^- \tag{14}$$

$$\text{Cathodic reaction:} \qquad 2\,H^+ + 2\,e^- \rightarrow H_2 \tag{15}$$

In this case Ir-based oxide are usually used as catalytic anode, while unsupported or of carbon-supported Pt particles are used at the cathode [156]. Unfortunately, iridium is extremely expensive and rare, around 0.5 kg of iridium is required per megawatt installed electrolyzer power [169]. Therefore, it is crucial to obtain a significant reduction of the catalyst loading. IrOx nanofibers have been combined with a conventional nanoparticle based IrOx anodic catalyst layer, resulting in an iridium loading reduction of over 80% while maintaining the same performance. This result has been attributed to a combination among the good electrical contact and high porosity of IrOx nanofibers with the high surface area of IrOx nanoparticles [169].

The most used polymer membranes for proton-exchange membrane water electrolysis are perfluorosulfonated acids, which are characterized by high proton conductivity, mechanical and chemical robustness. On the other hand, they are high-cost materials and

are characterized by significant gas permeability, low mechanical stability for temperature higher to 80 °C and present environmental issues due to the presence of fluorine. As alternative, sulfonated poly(phenylene sulfone) (sPPS) combines high proton conductivity with low gas crossover can be used. It has been reported that the performance of the sPPS-MEAs is substantially better than that of Nafion N115-MEAs (3.5 A·cm^{-2} vs 1.5 A·cm^{-2} at 1.8 V) with the same catalyst loading and comparable membrane thickness [170].

The effect of degradation on the performance of a PEM electrolysis cell has been investigated, at low catalyst loading, moreover, the degradation mechanism was investigated by means of ac-impedance spectra and post-operation analyses [171]. The results showed that the mass transfer issues are relevant under steady-state mode, while the catalyst degradation occurs under cycled operations. The membrane thinning depends on the uptime hours at high current density, while the overall cell voltage increase is higher for cycled operations than for steady-state mode, due to a higher decrease of series resistance in steady-state mode.

Porous transport layers (PTL) play a kay role in PEM water electrolysis cells, as it is involved in gas and liquid transport, in thermal and electrical conduction and in the contact between adjacent components [172], particularly those of the PTL surface in contact with the catalyst layer [173]. The actually used PTL are single layer sintered porous Ti-based materials, recently it has been reported that better performance can be achieved with multiple layers [174]. The catalyst loading affects the influence of PTL on the electrolysis performance, for low catalyst loading; moreover, at high current density, the apparent bubble coverage increased with PTL grain size at high catalyst loading [173]. The electrolysis performance are also related to the anode PTL properties, which can significantly impact ohmic, activation and diffusion losses [172]. By modifying the wettability of the PTL by adding hydrophobic additives, diffusion loss, ohmic loss and activation loss significantly increase.

5.4. Bipolar Membrane Electrolysis

One of the major limitations in the production of hydrogen by conventional water electrolysis, derives from the two semi-reactions of evolution of hydrogen and oxygen which, being simultaneous, are interdependent. Generally, the first reaction is fast in acidic conditions where there is an abundance of protons, while the second is slow, unless extremely expensive and rare catalysts such as iridium and ruthenium are used. A possible alternative is the amphoteric water electrolysis that, with a bipolar membrane, can provide optimal pH conditions simultaneously for both cathode and anode, under steady-state operations, without changing the overall thermodynamics of water splitting [175]. It has been shown that the decoupled amphoteric water electrolysis assisted with the redox mediator MnO_2/Mn^{2+}, by separating the production of hydrogen and oxygen into two independent processes, allows to produce hydrogen with a high-power input (up to 1 A·cm^{-2}), and low power absorbed oxygen production. Similar results were obtained with liquid water; in particular it has been reported that a bipolar membrane with and without a water splitting catalyst resulted in cell current densities of 450 and 5 mA·cm^{-2} at cell voltages of 2.2 V. Upon moving the bipolar interface directly between the acidic membrane and the high-pH anode, a current density of 9000 mA·cm^{-2} at cell voltages of 2.2 V was achieved [176].

5.5. Solid Oxide Electrolysis Cells

In solid oxide electrolysis cells (SOEC), a solid oxide or ceramic is used as electrolyte; at the cathode side hydrogen is produced from water (17), while the oxygen ions generated, across the electrolyte, reach the anode (16) where they are oxidized to produce oxygen:

$$\text{Anodic reaction:} \qquad 2O^{2-} \rightarrow O_2 + 4\,e^- \tag{16}$$

$$\text{Cathodic reaction:} \qquad H_2O + 2\,e^- \rightarrow H_2 + O^{2-} \tag{17}$$

The solid oxide electrolysis cells typically operate in the temperature range 500–900 °C [177], which provides a crucial benefit over proton exchange membrane (PEM) and alkaline exchange membrane (AEM) electrolyzers, which operate at a maximum of 100 °C. Unfortunately, the degradation of SOEC is the major limitation to the commercial viability, the aggressive humid condition in the air electrode side, is still a concern to the stability of electrolysis cells [178]. Typically, Ni/yttria-stabilized zirconia (Ni/YSZ) electrodes are used [179], however agglomeration of Ni nanoparticles, low water vapor transmission efficiency and poor durability are serious issues [180].

A series of studies have been focused on the optimization of the electrodes. An A-site cation-deficient $La_{0.4}Sr_{0.55}Co_{0.2}Fe_{0.6}Nb_{0.2}O_{3-d}$ perovskite has been recently reported, exhibiting a high electrolysis current density of 0.956 A·cm^{-2} with an applied voltage of 1.3 V at 850 °C and good stability in a high humidity and hydrogen partial pressure environment [180]. The high operating stability of the electrode has been attributed to the strong interaction between the alloy nanoparticles and the perovskite substrate, that suppresses the sintering of the nanoparticles, moreover the SrO phase is able to protect the alloy nanoparticles from oxidation.

A similar effect has been reported with barium doping, $Ba_{0.2}Sr_{1.8}Fe_{1.5}Mo_{0.5}O_{6-\delta}$ double perovskite as fuel electrode, which showed good performance with the appropriate steam amount of 20% [181].

The B-site of $Ba_{0-5}Sr_{0-5}Co_{0-8}Fe_{0-2}O_{3-\delta}$ of perovskite anode has been partially substituted with a higher valence Ta^{5+} (5, 10, 15 and 20 mol%) to improve the structural stability [182]. The current density of 10 mol% doped catalyst was 8.3 times higher than undoped one at 1.8 V, providing the higher of H_2 production rate, moreover, the degradation rate was 0.0027 V·h^{-1}, (−0.45 A·cm^{-2}, 800 °C, steam/H_2 = 70:30). It has been assumed that the Ta^{5+} doping provides a balance between ionic and electronic conductivity in the anode and a better electrochemical performance.

$BaCe_{0.5}Zr_{0.2}Y_{0.1}Yb_{0.1}Gd_{0.1}O_{3-\delta}$ (BCZYYbGd) electrolyte, characterized by high chemical stability and proton conductivity has been coupled with a $PrNi_{0.5}Co_{0.5}O_{3-\delta}$ steam electrode and a Ni-BCYYbGd hydrogen electrode for intermediate temperature operation (Figure 11) [183]. The BCYYbGd electrolyte showed high stability over 200 h at 50 vol % steam in argon and at 600 °C, moreover, high current density of 2.405 A·cm^{-2} at a cell voltage of 1.6 V was obtained at 600 °C at 20 vol % of steam in argon.

An effective way to improve the performance of the oxygen electrode is the infiltration, in which the electrocatalysts are introduced into a porous backbone at relatively low temperatures. $La_{0.6}Sr_{0.4}CoO_{3-\delta}$ (LSC) infiltrated gadolinia-doped ceria (CGO) oxygen electrode has been reported; in electrolysis mode, the current density reached 1.07 A·cm^{-2} at cell voltage of 1.3 V at 750 °C with a steam 60 vol% [184].

Symmetrical solid oxide cells configuration has also been evaluated, in which $Sr_2Fe_{1.5}Mo_{0.5}O_{6-\delta}$ electrodes are deposited on both sides of YbScSZ tapes previously coated with a $Ce_{1-x}Gd_xO_{1.9}$ [185]. This configuration has shown some advantages such as a reduction of sintering steps or a better thermomechanical compatibility between the electrodes and the electrolyte.

The electrochemical performance of cathode-supported cells having gadolinium doped ceria/yttria-stabilized zirconia (GDC/YSZ), yttria-stabilized zirconia (YSZ) and Sc^{3+}, Ce^{4+}, and Gd^{3+}-doped zirconia (SCGZ) electrolyte was compared, highlighting the highest electrochemical performance of the cathode-supported cell having SCGZ electrolyte (Ni-SCGZ/SCGZ/BSCF) [186].

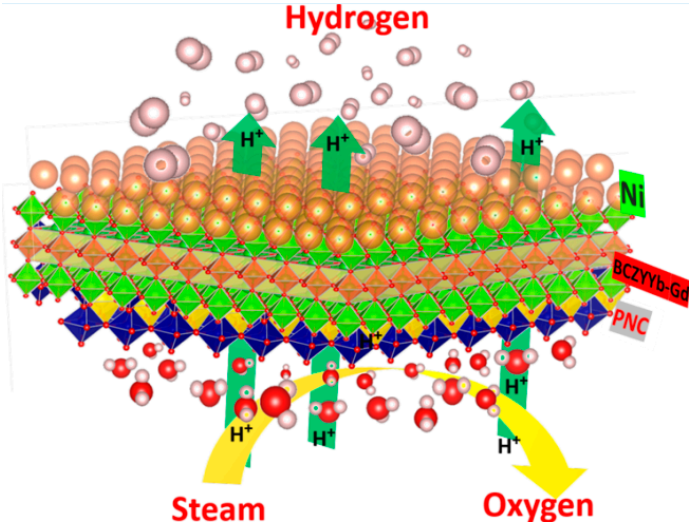

Figure 11. Representation of the solid oxide electrolysis cell [183].

A heterogeneous design for proton-conducting solid oxide electrolysis cells has also been proposed, in which a better stability and higher efficiency of electrolysis cells has been obtained [178]. Yttrium and zirconium co-doped barium cerate-nickel was used as fuel electrode material and yttrium-doped barium zirconate as the electrolyte material. The results showed that the proposed novel design can efficiently improve the proton conductivity of the yttrium-doped barium zirconate electrolyte (from 0.88×10^{-3} S·cm^{-1} to 2.13×10^{-3} S·cm^{-1} at 600 °C) and improve the ionic transport number of the electrolyte (from 0.941 to 0.964 at 600 °C).

5.6. Reamarks on Electrical Methods

The hydrogen production from electrolyzers is a mature technology, and among the electrochemical technology, alkaline water electrolysis is already available for large-scale applications, due to the use of non-expensive materials for the electrodes [187]. The use of renewable energy is a necessary boundary condition, however there is a problem with a partial loading when renewable energy supply is intermittent and unstable. An energy storage device can partially solve the incompatibility between water electrolyzers and renewable energy sources. The process can be efficient if the electrolyser is powered, for example, by solar photovoltaic through a full cell of lithium-ion battery as an energy reservoir [188]. On the other hand, solid oxide electrolysis cells are extremely attractive, due to the possibility to work at high temperatures where higher efficiency can be reached. Although the critical issues related to the stability of these cells have not yet been solved, it has been demonstrated that a plant in which the SOEC is integrated with a parabolic dish solar field, to provide both electricity and thermal energy, necessary for the electrolysis reaction to take place, a nominal solar-to-hydrogen efficiency above 30%, with a SOEC efficiency around 80%, can be reached [189]. In another study it has been calculated that is possible to produce hydrogen in electrolyzers integrated with nuclear plants with an energy cost of 38.83 and 37.55 kWh·kg_{H2}^{-1} for protonic and ionic solid oxide electrolyzers, respectively [190].

6. Economic Assessment

Establishing the costs of hydrogen per type of production process is outside the scope of this article, however it is possible to make an approximate assessment based on what is reported in the literature. Evaluating the costs of production processes based on immature techniques is extremely difficult and risky, as the costs are related to diffusion. In any case, however, various costs, capital and operating costs, design, labor, electricity, as well as the costs of raw materials, waste disposal etc. must be considered. In the case

of biological and photonic methods, dark fermentation is most promising technology, with estimated hydrogen production costs in the range of 1.02–2.70 USD m^{-3} and a high return on investment (calculated as the ratio between annual profit and fixed capital investment) [155]. The hydrogen production cost via natural gas steam reforming is equal to 0.67 USD m^{-3}, however with a lower return on investment. The hydrogen production cost in the case of electrolysis is strongly dependent on the electricity cost, for example in Germany is around 3.64 €q Kg^{-1}, for alkaline water electrolysers. At the moment, therefore, the lowest costs are found in the case of natural gas reforming, however these assessments lack environmental costs, which could substantially modify the results reported so far.

7. Conclusions and Future Prospective

Hydrogen is the most promising energy carrier; however, it is scarcely present in Nature in molecular form, therefore it must be obtained from primary sources. In this review article, the main characteristics of a number of hydrogen production methods have been listed, focusing primarily on renewable feedstock. The production methods have been grouped into three main sections, based on the type of energy used to sustain the process. For each section, the main limitations to the diffusion of the analysed production processes have been highlighted. As mentioned, the most widespread hydrogen production methods are, still today, natural gas reforming processes, which use feedstock abundantly available at low cost, and use proven processes. However, the need to achieve carbon neutrality requires the use of renewable feedstock and energy to support production processes.

Water is the main source of hydrogen, via water splitting processes, however the enormous amount of energy required to support these constitutes a serious limitation, and therefore the use of energy from renewable sources is a necessary boundary condition. Among the various techniques, alkaline electrolysis of water is now available for large-scale applications. On the other hand, biomasses are extremely attractive; as a variety of materials such as algae, food waste, municipal solid waste, lignocellulosic biomass etc. can be used. Several processes can be used to obtain hydrogen from biomass, such as gasification and fermentation, furthermore bio-oils, obtained by pyrolysis of biomass and the same of biomethane, can be used in reforming processes. The main limitations to their use seem to be the variability of the composition and therefore the unavailability of large quantities at low cost.

The origin of the energy needed to sustain the processes itself plays a crucial role. In this context, electrification can make sustainable the processes that use thermal methods. However, the main problem related to the use of renewable energy is the instability in the supply which, in many cases, is intermittent.

Based on these considerations, a future is outlined increasingly based on the local production and distribution of energy and therefore of hydrogen, in which the decentralization of hydrogen production will play a key role. The energy to support the processes must be generated on site, exploiting the potential of the territory, such as wind power, solar power, etc. Likewise, the feedstock for hydrogen production will have to be available where hydrogen will be produced. A massive use of biomass will make it necessary to implement processes that are tolerant to the variability of the biomass itself, so as to minimize production costs.

Author Contributions: All authors equally contributed to the conceptualization, methodology, software, validation, formal analysis, investigation, resources, data curation, writing-original draft preparation, writing-review and editing, visualization, supervision, project administration and funding acquisition of this manuscript. All authors have read and agreed to the published version of the manuscript.

Funding: This work has received funding from the European Union's Horizon 2020 research and innovation programme under the Marie Skłodowska-Curie grant agreement No 734561.

Acknowledgments: The authors wish to acknowledge Ing. Antonio Corrado for the valuable contribution on the electrification of reforming processes.

Conflicts of Interest: The authors declare no conflict of interest.

References

1. Available online: https://www.un.org/press/en/2012/sgsm14242.doc.htm (accessed on 20 April 2012).
2. Jeuland, M.; Fetter, T.R.; Li, Y.; Pattanayak, S.K.; Usmani, F.; Bluffstone, R.A.; Chávez, C.; Girardeau, H.; Hassen, S.; Jagger, P.; et al. Is energy the golden thread? A systematic review of the impacts of modern and traditional energy use in low- and middle-income countries. *Renew. Sust. Energ. Rev.* **2021**, *135*, 110406. [CrossRef]
3. *Special Report: Global Warming of 1.5 °C*; Intergovernmental Panel on Climate Change: Geneva, Switzerland, 2018. Available online: https://www.ipcc.ch/sr15/ (accessed on 12 March 2020).
4. Marnellos, G.E.; Klassen, T. Welcome to Hydrogen—A New International and Interdisciplinary Open Access Journal of Growing Interest in Our Society. *Hydrogen* **2020**, *1*, 6. [CrossRef]
5. Available online: https://www.europarl.europa.eu/news/en/headlines/society/20190926STO62270/what-is-carbon-neutrality-and-how-can-it-be-achieved-by-2050 (accessed on 8 October 2020).
6. Available online: https://www.e-education.psu.edu/earth104/node/1345 (accessed on 1 February 2021).
7. Abdin, Z.; Zafaranloo, A.; Rafee, A.; Mérida, W.; Lipiński, W.; Khalilpour, K.R. Hydrogen as an energy vector. *Ren. Sust. Energ. Rev.* **2020**, *120*, 109620. [CrossRef]
8. Boyle, R. *Tracts, Containing New Experiments, Touching the Relation betwixt Flame and Air*; Richard Davis: London, UK, 1672.
9. Available online: https://www.thoughtco.com/most-abundant-element-in-known-space-4006866 (accessed on 7 April 2021).
10. Safari, F.; Dincer, I. A review and comparative evaluation of thermochemical water splitting cycles for hydrogen production. *Energy Convers. Manag.* **2020**, *205*, 112182. [CrossRef]
11. Rambhujun, N.; Salman, M.S.; Wang, T.; Pratthana, C.; Sapkota, P.; Costalin, M.; Lai, Q.; Aguey-Zinsou, K.-F. Renewable hydrogen for the chemical industry. *Mrs Energy Sustain.* **2020**, *7*, E33. [CrossRef]
12. Dawood, F.; Anda, M.; Shafiullah, G.M. Hydrogen production for energy: An overview. *Int. J. Hydrogen Energy* **2020**, *45*, 3847–3869. [CrossRef]
13. Shen, Q.; Jiang, Y.; Xia, F.; Wang, B.; Lv, X.; Ye, W.; Yang, G. Hydrogen production by Co-based bimetallic nano-catalysts and their performance in methane steam reforming. *Pet. Sci. Technol.* **2020**, *38*, 618–625. [CrossRef]
14. Chen, L.; Qi, Z.; Zhang, S.; Su, J.; Somorjai, G.A. Catalytic Hydrogen Production from Methane: A Review on Recent Progress and Prospect. *Catalysts* **2020**, *10*, 858. [CrossRef]
15. Palma, V.; Gallucci, F.; Pullumbi, P.; Ruocco, C.; Meloni, E.; Martino, M. Pt/Re/CeO_2 Based Catalysts for CO-Water–Gas Shift Reaction: From Powders to Structured Catalyst. *Catalysts* **2020**, *10*, 564. [CrossRef]
16. Palma, V.; Ruocco, C.; Cortese, M.; Renda, S.; Meloni, E.; Festa, G.; Martino, M. Platinum Based Catalysts in the Water Gas Shift Reaction: Recent Advances. *Metals* **2020**, *10*, 866. [CrossRef]
17. Palma, V.; Ruocco, C.; Cortese, M.; Martino, M. Recent Advances in Structured Catalysts Preparation and Use in Water-Gas Shift Reaction. *Catalysts* **2019**, *9*, 991. [CrossRef]
18. Garbis, P.; Jess, A. Selective CO Methanation in H_2-Rich Gas for Household Fuel Cell Applications. *Energies* **2020**, *13*, 2844. [CrossRef]
19. Jiang, Z.; Liao, M.; Qi, J.; Wang, C.; Chen, Y.; Luo, X.; Liang, B.; Shu, R.; Song, Q. Enhancing hydrogen production from propane partial oxidation via CO preferential oxidation and CO_2 sorption towards solid oxide fuel cell (SOFC) applications. *Renew. Energy* **2020**, *156*, 303–313. [CrossRef]
20. Tosto, E.; Alique, D.; Martinez-Diaz, D.; Sanz, R.; Calles, J.A.; Caravella, A.; Medrano, J.A.; Gallucci, F. Stability of pore-plated membranes for hydrogen production in fluidized-bed membrane reactors. *Int. J. Hydrogen Energy* **2020**, *45*, 7374–7385. [CrossRef]
21. Meloni, E.; Martino, M.; Palma, V. A Short Review on Ni Based Catalysts and Related Engineering Issues for Methane Steam Reforming. *Catalysts* **2020**, *10*, 352. [CrossRef]
22. Gray, J.T.; Che, F.; McEwen, J.-S.; Ha, S. Field-assisted suppression of coke in the methane steam reforming reaction. *Appl. Catal. B-Environ.* **2020**, *260*, 118132. [CrossRef]
23. Palma, V.; Meloni, E.; Renda, S.; Martino, M. Catalysts for Methane Steam Reforming Reaction: Evaluation of CeO_2 Addition to Alumina-Based Washcoat Slurry Formulation. *C J. Carbon Res.* **2020**, *6*, 52. [CrossRef]
24. Han, B.; Wang, F.; Zhang, L.; Wang, Y.; Fan, W.; Xu, L.; Yu, H.; Li, Z. Syngas production from methane steam reforming and dry reforming reactions over sintering-resistant Ni@SiO_2 catalyst. *Res. Chem. Intermed.* **2020**, *46*, 1735–1748. [CrossRef]
25. Balzarotti, R.; Ambrosetti, M.; Beretta, A.; Groppi, G.; Tronconi, E. Investigation of packed conductive foams as a novel reactor configuration for methane steam reforming. *Chem. Eng. J.* **2020**, *391*, 123494. [CrossRef]
26. Renda, S.; Cortese, M.; Iervolino, G.; Martino, M.; Meloni, E.; Palma, V. Electrically driven SiC-based structured catalysts for intensified reforming processes. *Catal. Today* **2020**. [CrossRef]
27. Meloni, E.; Martino, M.; Ricca, A.; Palma, V. Ultracompact methane steam reforming reactor based on microwaves susceptible structured catalysts for distributed hydrogen production. *Int. J. Hydrogen Energy* **2021**, *46*, 13729–13747. [CrossRef]
28. Grasham, O.; Dupont, V.; Cockerill, T.; Alonso Camargo-Valero, M.; Twigg, M.V. Hydrogen via reforming aqueous ammonia and biomethane co-products of wastewater treatment: Environmental and economic sustainability. *Sustain. Energy Fuels* **2020**, *4*, 5835–5850. [CrossRef]

29. Zhang, L.; Yu, Z.; Li, J.; Zhang, S.; Hu, S.; Xiang, J.; Wang, Y.; Liu, Q.; Hu, G.; Hu, X. Steam reforming of typical small organics derived from bio-oil: Correlation of their reaction behaviors with molecular structures. *Fuel* **2020**, *259*, 116214. [CrossRef]
30. Megía, P.J.; Calles, J.A.; Carrero, A.; Vizcaíno, A.J. Effect of the incorporation of reducibility promoters (Cu, Ce, Ag) in Co/CaSBA-15 catalysts for acetic acid steam reforming. *Int. J. Energy Res.* **2021**, *45*, 1685–1702. [CrossRef]
31. Li, J.; Mei, X.; Zhang, L.; Yu, Z.; Liu, Q.; Wei, T.; Wu, W.; Dong, D.; Xu, L.; Hu, X. A comparative study of catalytic behaviors of Mn, Fe, Co, Ni, Cu and ZneBased catalysts in steam reforming of methanol, acetic acid and acetone. *Int. J. Hydrogen Energy* **2020**, *45*, 3815–3832. [CrossRef]
32. Palma, V.; Ruocco, C.; Cortese, M.; Martino, M. Bioalcohol Reforming: An Overview of the Recent Advances for the Enhancement of Catalyst Stability. *Catalysts* **2020**, *10*, 665. [CrossRef]
33. Hou, X.; Qing, S.; Liu, Y.; Li, L.; Gao, Z.; Qin, Y. Enhancing effect of MgO modification of Cu-Al spinel oxide catalyst for methanol steam reforming. *Int. J. Hydrogen Energy* **2020**, *45*, 477–489. [CrossRef]
34. Azenha, C.; Lagarteira, T.; Mateos-Pedrero, C.; Mendes, A. Production of hydrogen from methanol steam reforming using CuPd/ZrO_2 catalysts—Influence of the catalytic surface on methanol conversion and CO selectivity. *Int. J. Hydrogen Energy* **2020**. [CrossRef]
35. López-Martín, A.; Platero, F.; Caballero, A.; Colón, G. Thermo-Photocatalytic Methanol Reforming for Hydrogen Production over a CuPd-TiO_2 Catalyst. *ChemPhotoChem* **2020**, *4*, 630–637. [CrossRef]
36. Yu, C.-L.; Sakthinathan, S.; Hwang, B.-Y.; Lin, S.-Y.; Chiu, T.-W.; Yu, B.-S.; Fan, Y.-J.; Chuang, C. $CuFeO_2$-CeO_2 nanopowder catalyst prepared by self-combustion glycine nitrate process and applied for hydrogen production from methanol steam reforming. *Int. J. Hydrogen Energy* **2020**, *45*, 15752–15762. [CrossRef]
37. Yu, H.; Xu, C.; Li, Y.; Jin, F.; Ye, F.; Li, X. Performance Enhancement of CuO/ZnO by Deposition on the Metal-Organic Framework of Cu-BTC for Methanol Steam Reforming Reaction. *ES Energy Environ.* **2020**, *8*, 65–77. [CrossRef]
38. Kovalskiia, A.M.; Matveev, A.T.; Popov, Z.I.; Volkov, I.N.; Sukhanova, E.V.; Lytkina, A.A.; Yaroslavtsev, A.B.; Konopatsky, A.S.; Leybo, D.V.; Bondarev, A.V.; et al. (Ni,Cu)/hexagonal BN nanohybrids—New efcient catalysts for methanol steam reforming and carbon monoxide oxidation. *Chem. Eng. J.* **2020**, *395*, 125109. [CrossRef]
39. Mateos-Pedreroa, C.; Azenha, C.; Pacheco Tanaka, D.A.; Sousa, J.M.; Mendes, A. The influence of the support composition on the physicochemical and catalytic properties of Cu catalysts supported on Zirconia-Alumina for methanol steam reforming. *Appl. Catal. B-Environ.* **2020**, *277*, 119243. [CrossRef]
40. Khani, Y.; Kamyar, N.; Bahadoran, F.; Safari, N.; Amini, M.M. A520 MOF-derived alumina as unique support for hydrogen production from methanol steam reforming: The critical role of support on performance. *Renew. Energy* **2020**, *156*, 1055–1064. [CrossRef]
41. Fasanya, O.O.; Atta, A.Y.; Myint, M.T.Z.; Dutta, J.; Jibril, B.Y. Effects of synthesis methods on performance of CuZn/MCM-41 catalysts in methanol steam reforming. *Int. J. Hydrogen Energy* **2021**, *46*, 3539–3553. [CrossRef]
42. Song, Q.; Men, Y.; Wang, J.; Liu, S.; Chai, S.; An, W.; Wang, K.; Li, Y.; Tang, Y. Methanol steam reforming for hydrogen production over ternary composite $ZnyCe_1Zr_9O_X$ catalysts. *Int. J. Hydrogen Energy* **2020**, *45*, 9592–9602. [CrossRef]
43. Cai, F.; Juweriah Ibrahim, J.; Fu, Y.; Kong, W.; Zhang, J.; Sun, Y. Low-temperature hydrogen production from methanol steam reforming on Zn-modified Pt/MoC catalysts. *Appl. Catal. B-Environ.* **2020**, *264*, 118500. [CrossRef]
44. Köwitsch, N.; Thoni, L.; Klemmed, B.; Benad, A.; Paciok, P.; Heggen, M.; Köwitsch, I.; Mehring, M.; Eychmüller, A.; Armbrüster, M.; et al. Proving a Paradigm in Methanol Steam Reforming: Catalytically Highly Selective InxPdy/In_2O_3 Interfaces. *ACS Catal.* **2021**, *11*, 304–312. [CrossRef]
45. Ogo, S.; Sekine, Y. Recent progress in ethanol steam reforming using non-noble transition metal catalysts: A review. *Fuel Proces. Technol.* **2020**, *199*, 106238. [CrossRef]
46. Yoo, S.; Park, S.; Song, J.H.; Kim, D.H. Hydrogen production by the steam reforming of ethanol over K-promoted Co/Al_2O_3–CaO xerogel catalysts. *Mol. Catal.* **2020**, *491*, 110980. [CrossRef]
47. Martinelli, M.; Watson, C.D.; Jacobs, G. Sodium doping of Pt/m-ZrO_2 promotes C-C scission and decarboxylation during ethanol steam reforming. *Int. J. Hydrogen Energy* **2020**, *45*, 18490–18501. [CrossRef]
48. Vecchietti, J.; Lustemberg, P. Controlled selectivity for ethanol steam reforming reaction over doped CeO_2 surfaces: The role of gallium. *Appl. Catal. B-Environ.* **2020**, *277*, 119103. [CrossRef]
49. Greluk, M.; Rotko, M.; Turczyniak-Surdacka, S. Enhanced catalytic performance of La_2O_3 promoted Co/CeO_2 and Ni/CeO2 catalysts for effective hydrogen production by ethanol steam reforming. *Renew. Energy* **2020**, *155*, 378–395. [CrossRef]
50. Li, Y.; Zhang, Z.; Jia, P.; Dong, D.; Wang, Y.; Hu, S.; Xiang, J.; Liu, Q.; Hu, X. Ethanol steam reforming over cobalt catalysts: Effect of a range of additives on the catalytic behaviors. *J. Energy Inst.* **2020**, *93*, 165–184. [CrossRef]
51. Dai, R.; Zheng, Z.; Yan, W.; Lian, C.; Wu, X.; An, X.; Xie, X. Dragon fruit-like Pt-Cu@mSiO_2 nanocomposite as an efficient catalyst for low-temperature ethanol steam reforming. *Chem Eng. J.* **2020**, *379*, 122299. [CrossRef]
52. Chen, D.; Liu, C.; Mao, Y.; Wang, W.; Li, T. Efficient hydrogen production from ethanol steam reforming over layer-controlled graphene-encapsulated Ni catalysts. *J. Clean. Prod.* **2020**, *252*, 119907. [CrossRef]
53. Smal, E.A.; Simonov, M.N.; Mezentseva, N.V.; Krieger, T.A.; Larina, T.V.; Saraev, A.A.; Glazneva, T.S.; Ishchenko, A.V.; Rogov, V.A.; Eremeev, N.F.; et al. Spinel-type $MnxCr_{3-x}O_4$-based catalysts for ethanol steam reforming. *Appl. Catal. B-Environ.* **2021**, *283*, 119656. [CrossRef]

54. Afolabi, A.T.F.; Kechagiopoulos, P.N.; Liu, Y.; Li, C.-Z. Kinetic features of ethanol steam reforming and decomposition using a biochar-supported Ni catalyst. *Fuel Proces. Technol.* **2021**, *212*, 106622. [CrossRef]
55. Charisiou, N.D.; Siakavelas, G.I.; Papageridis, K.N.; Motta, D.; Dimitratos, N.; Sebastian, V.; Polychronopoulou, K.; Goula, M.A. The Effect of Noble Metal (M: Ir, Pt, Pd) on M/Ce_2O_3-γ-Al_2O_3 Catalysts for Hydrogen Production via the Steam Reforming of Glycerol. *Catalysts* **2020**, *10*, 790. [CrossRef]
56. Asmawati Roslan, N.; Zainal Abidin, S.; Ideris, A.; Vo, D.-V.N. A review on glycerol reforming processes over Ni-based catalyst for hydrogen and syngas productions. *Int. J. Hydrogen Energy* **2020**, *45*, 18466–18489. [CrossRef]
57. Charisiou, N.D.; Italiano, C.; Pino, L.; Sebastian, V.; Vita, A.; Goula, M.A. Hydrogen production via steam reforming of glycerol over Rh/ɣ-Al_2O_3 catalysts modified with CeO_2, MgO or La_2O_3. *Renew. Energy* **2020**, *162*, 908–925. [CrossRef]
58. Ghaffari Saeidabad, N.; Noh, Y.S.; Alizadeh Eslami, A.; Song, H.T.; Kim, H.D.; Fazeli, A.; Moon, D.J. A Review on Catalysts Development for Steam Reforming of Biodiesel Derived Glycerol; Promoters and Supports. *Catalysts* **2020**, *10*, 910. [CrossRef]
59. Feng, P.; Huang, K.; Xu, Q.; Qi, W.; Xin, S.; Wei, T.; Liao, L.; Yan, Y. Ni supported on the CaO modified attapulgite as catalysts for hydrogen production from glycerol steam reforming. *Int. J. Hydrogen Energy* **2020**, *45*, 8223–8233. [CrossRef]
60. Yancheshmeh, M.S.; Sahraei, O.A.; Aissaoui, M.; Iliuta, M.C. A novel synthesis of $NiAl_2O_4$ spinel from a Ni-Al mixed-metal alkoxide as a highly efficient catalyst for hydrogen production by glycerol steam reforming. *Appl. Catal. B-Environ.* **2020**, *265*, 118535. [CrossRef]
61. Moogi, S.; Nakka, L.; Prasad Potharaju, S.S.; Ahmed, A.; Farooq, A.; Jung, S.-C.; Hoon Rhee, G.; Park, Y.-K. Copper promoted Co/MgO: A stable and efficient catalyst for glycerol steam reforming. *Int. J. Hydrogen Energy* **2020**. [CrossRef]
62. Wang, R.; Liu, S.; Liu, S.; Li, X.; Zhang, Y.; Xie, C.; Zhou, S.; Qiu, Y.; Luo, S.; Jing, F.; et al. Glycerol steam reforming for hydrogen production over bimetallic MNi/CNTs (M = Co, Cu and Fe) catalysts. *Catal. Today* **2020**, *355*, 128–138. [CrossRef]
63. Conte, F.; Esposito, S.; Dal Santo, V.; Di Michele, A.; Ramis, G.; Rossetti, I. Flame Pyrolysis Synthesis of Mixed Oxides for Glycerol Steam Reforming. *Materials* **2021**, *14*, 652. [CrossRef] [PubMed]
64. Matus, E.V.; Ismagilov, I.Z.; Yashnik, S.A.; Ushakov, V.A.; Prosvirin, I.P.; Kerzhentsev, M.A.; Ismagilov, Z.R. Hydrogen production through autothermal reforming of CH_4: Efficiency and action mode of noble (M = Pt, Pd) and non-noble (M = Re, Mo, Sn) metal additives in the composition of Ni-$M/Ce_{0.5}Zr_{0.5}O_2/Al_2O_3$ catalysts. *Int. J. Hydrogen Energy* **2020**, *45*, 33352–33369. [CrossRef]
65. Osazuwa, O.U.; Abidin, S.Z.; Fan, X.; Nosakhare Amenaghawon, A.; Azizan, T.M. An insight into the effects of synthesis methods on catalysts properties for methane reforming. *J. Environ. Chem. Eng.* **2021**, *9*, 105052. [CrossRef]
66. Mosinska, M.; Stępińska, N.; Maniukiewicz, W.; Rogowski, J.; Mierczynska-Vasilev, A.; Vasilev, K.; Szynkowska, M.I.; Mierczynski, P. Hydrogen Production on Cu-Ni Catalysts via the Oxy-Steam Reforming of Methanol. *Catalysts* **2020**, *10*, 273. [CrossRef]
67. Sun, Z.; Zhang, X.; Li, H.; Sang, S.; Chen, S.; Duan, L.; Zeng, L.; Xiang, W.; Gong, J. Chemical looping oxidative steam reforming of methanol: A new pathway for auto-thermal conversion. *Appl. Catal. B-Environ.* **2020**, *269*, 118758. [CrossRef]
68. Rodríguez Lugo, V.; Mondragon-Galicia, G.; Gutiérrez-Martínez, A.; Gutiérrez-Wing, C.; González, O.R.; López, P.; Salinas-Hernández, P.; Tzompantzi, F.; Valderrama, M.I.R.; Pérez-Hernández, R. Pt–Ni/ZnO-rod catalysts for hydrogen production by steam reforming of methanol with oxygen. *RSC Adv.* **2020**, *10*, 41315. [CrossRef]
69. Ruocco, C.; Palma, V.; Cortese, M.; Martino, M. Noble Metals-Based Catalysts for Hydrogen Production via Bioethanol Reforming in a Fluidized Bed Reactor. *Chem. Proc.* **2020**, *2*, 7543. [CrossRef]
70. Pio, G.; Ruocco, C.; Palma, V.; Salzano, E. Detailed kinetic mechanism for the hydrogen production via the oxidative reforming of ethanol. *Chem. Eng. Sci.* **2021**, *237*, 116591. [CrossRef]
71. Cao, L.; Yu, I.K.M.; Xiong, X.; Tsang, D.C.W.; Zhang, S.; Clark, J.H.; Hu, C.; Ng, Y.H.; Shang, J.; Ok, Y.S. Biorenewable hydrogen production through biomass gasification: A review and future prospects. *Environ. Res.* **2020**, *186*, 109547. [CrossRef]
72. Singh Siwal, S.; Zhang, Q.; Sun, C.; Thakur, S.; Kumar Gupta, V.; Kumar Thakur, V. Energy production from steam gasification processes and parameters that contemplate in biomass gasifier—A review. *Bioresour. Technol.* **2020**, *297*, 122481. [CrossRef] [PubMed]
73. AlNouss, A.; McKay, G.; Al-Ansari, T. Production of syngas via gasification using optimum blends of biomass. *J. Clean. Prod.* **2020**, *242*, 118499. [CrossRef]
74. Wang, C.; Jin, H.; Feng, H.; Wei, W.; Cao, C.; Cao, W. Study on gasification mechanism of biomass waste in supercritical water based on product distribution. *Int. J. Hydrogen Energy* **2020**, *45*, 28051–28061. [CrossRef]
75. Chen, J.; Fan, Y.; Zhao, X.; E, J.; Xu, W.; Zhang, F.; Liao, G.; Leng, E.; Liu, S. Experimental investigation on gasification characteristic of food waste using supercritical water for combustible gas production: Exploring the way to complete gasification. *Fuel* **2020**, *263*, 116735. [CrossRef]
76. Mehrpooya, M.; Habibi, R. A review on hydrogen production thermochemical water-splitting cycles. *J. Clean. Prod.* **2020**, *275*, 123836. [CrossRef]
77. Gao, Y.; Mao, Y.; Song, Z.; Zhao, X.; Sun, J.; Wang, W.; Chen, G.; Chen, S. Efficient generation of hydrogen by two-step thermochemical cycles: Successive thermal reduction and water splitting reactions using equal-power microwave irradiation and a high entropy material. *Appl. Energy* **2020**, *279*, 115777. [CrossRef]
78. Safari, F.; Dincer, I. A study on the Fe-Cl thermochemical water splitting cycle for hydrogen production. *Int. J. Hydrogen Energy* **2020**, *45*, 18867–18875. [CrossRef]

79. Ngoensawata, A.; Tongnana, V.; Laosiripojanab, N.; Kim-Lohsoontornc, P.; Hartley, U.W. Effect of La and Gd substitution in $BaFeO_{3-\delta}$ perovskite structure on its catalytic performance for thermochemical water splitting. *Catal. Commun.* **2020**, *135*, 105901. [CrossRef]
80. Qian, X.; He, J.; Mastronardo, E.; Baldassarri, B.; Wolverton, C.; Haile, S.M. Favorable Redox Thermodynamics of $SrTi_{0.5}Mn_{0.5}O_{3-\delta}$ in Solar Thermochemical Water Splitting. *Chem. Mater.* **2020**, *32*, 9335–9346. [CrossRef]
81. Orfila, M.; Sanz, D.; Linares, M.; Molina, R.; Sanz, R.; Marugan, J.; Botas, J.A. H_2 production by thermochemical water splitting with reticulated porous structures of ceria-based mixed oxide materials. *Int. J. Hydrogen Energy* **2020**. [CrossRef]
82. Wang, Y.; Hong, Z.; Mei, D. A thermally autonomous methanol steam reforming microreactor with porous copper foam as catalyst support for hydrogen production. *Int. J. Hydrogen Energy* **2021**. [CrossRef]
83. Du, W.; Lee, M.-T.; Wang, Y.; Zhao, C.; Li, G.; Li, M. Design of a solar-driven methanol steam reforming receiver/reactor with a thermal storage medium and its performance analysis. *Int. J. Hydrogen Energy* **2020**, *45*, 33076–33087. [CrossRef]
84. da Fonseca Dias, V.; Dias da Silva, J. Mathematical modelling of the solar-driven steam reforming of methanol for a solar thermochemical micro-fuidized bed reformer: Thermal performance and thermochemical conversion. *J. Braz. Soc. Mec. Sci.* **2020**, *42*, 447. [CrossRef]
85. Chen, X.; Zhou, H.; Yu, Z.; Li, W.; Tang, J.; Xu, C.; Ding, Y.; Wan, Z. Thermodynamic and economic assessment of a PEMFC-based micro-CCHP system integrated with geothermal-assisted methanol reforming. *Int. J. Hydrogen Energy* **2020**, *45*, 958–971. [CrossRef]
86. Xu, Y.; Lu, B.; Luo, C.; Chen, J.; Zhang, Z.; Zhang, L. Sorption enhanced steam reforming of ethanol over Ni-based catalyst coupling with high-performance CaO pellets. *Chem. Eng. J.* **2021**, *406*, 126903. [CrossRef]
87. Jia, H.; Xu, H.; Sheng, X.; Yang, X.; Shen, W.; Goldbach, A. High-temperature ethanol steam reforming in PdCu membrane reactor. *J. Memb. Sci.* **2020**, *605*, 118083. [CrossRef]
88. Antonini, C.; Treyer, K.; Streb, A.; van der Spek, M.; Bauer, C.; Mazzotti, M. Hydrogen production from natural gas and biomethane with carbon capture and storage—A techno-environmental analysis. *Sustain. Energy Fuels* **2020**, *4*, 2967–2986. [CrossRef]
89. Lim, Y.; Lee, D.-K.; Kim, S.M.; Park, W.; Cho, S.Y.; Sim, U. Low Dimensional Carbon-Based Catalysts for Efficient Photocatalytic and Photo/Electrochemical Water Splitting Reactions. *Materials* **2020**, *13*, 114. [CrossRef]
90. Li, J.; Jiménez-Calvo, P.; Paineau, E.; Nawfal Ghazzal, M. Metal Chalcogenides Based Heterojunctions and Novel Nanostructures for Photocatalytic Hydrogen Evolution. *Catalysts* **2020**, *10*, 89. [CrossRef]
91. Enesca, A.; Andronic, L. Photocatalytic Activity of S-Scheme Heterostructure for Hydrogen Production and Organic Pollutant Removal: A Mini-Review. *Nanomaterials* **2021**, *11*, 871. [CrossRef]
92. Lettieri, S.; Pavone, M.; Fioravanti, A.; Santamaria Amato, L.; Maddalena, P. Charge Carrier Processes and Optical Properties in TiO_2 and TiO_2-Based Heterojunction Photocatalysts: A Review. *Materials* **2021**, *14*, 1645. [CrossRef] [PubMed]
93. Rusinque, B.; Escobedo, S.; de Lasa, H. Photoreduction of a Pd-Doped Mesoporous TiO_2 Photocatalyst for Hydrogen Production under Visible Light. *Catalysts* **2020**, *10*, 74. [CrossRef]
94. Rusinque, B.; Escobedo, S.; de Lasa, H. Hydrogen Production via Pd-TiO_2 Photocatalytic Water Splitting under Near-UV and Visible Light: Analysis of the Reaction Mechanism. *Catalysts* **2021**, *11*, 405. [CrossRef]
95. Wang, Z.; Fan, J.; Cheng, B.; Yu, J.; Xu, J. Nickel-based cocatalysts for photocatalysis: Hydrogen evolution, overall water splitting and CO_2 reduction. *Mat. Today Phys.* **2020**, *15*, 100279. [CrossRef]
96. Ayala, P.; Giesriegl, A.; Nandan, S.P.; Nagaraju Myakala, S.; Wobrauschek, P.; Cherevan, A. Isolation Strategy towards Earth-Abundant Single-Site Co-Catalysts for Photocatalytic Hydrogen Evolution Reaction. *Catalysts* **2021**, *11*, 417. [CrossRef]
97. Hampel, B.; Pap, Z.; Sapi, A.; Szamosvolgyi, A.; Baia, L.; Hernadi, K. Application of TiO_2-Cu Composites in Photocatalytic Degradation Different Pollutants and Hydrogen Production. *Catalysts* **2020**, *10*, 85. [CrossRef]
98. Potapenko, K.O.; Kurenkova, A.Y.; Bukhtiyarov, A.V.; Gerasimov, E.Y.; Cherepanova, S.V.; Kozlova, E.A. Comparative Study of the Photocatalytic Hydrogen Evolution over Cd1-xMnxS and CdS-β-Mn_3O_4-MnOOH Photocatalysts under Visible Light. *Nanomaterials* **2021**, *11*, 355. [CrossRef]
99. Xing, X.; Tang, S.; Hong, H.; Jin, H. Concentrated solar photocatalysis for hydrogen generation from water by titania-containing gold nanoparticles. *Int. J. Hydrogen Energy* **2020**, *45*, 9612–9623. [CrossRef]
100. Khabirul Islam, A.K.M.; Dunlop, P.S.M.; Hewitt, N.J.; Lenihan, R.; Brandoni, C. Bio-Hydrogen Production from Wastewater: A Comparative Study of Low Energy Intensive Production Processes. *Clean Technol.* **2021**, *3*, 10. [CrossRef]
101. Wei, Z.; Liu, J.; Shangguan, W. A review on photocatalysis in antibiotic wastewater: Pollutant degradation and hydrogen production. *Chin. J. Catal.* **2020**, *41*, 1440–1450. [CrossRef]
102. Armenise, V.; Colella, S.; Fracassi, F.; Listorti, A. Lead-Free Metal Halide Perovskites for Hydrogen Evolution from Aqueous Solutions. *Nanomaterials* **2021**, *11*, 433. [CrossRef] [PubMed]
103. Bahadori, E.; Ramis, G.; Zanardo, D.; Menegazzo, F.; Signoretto, M.; Gazzoli, D.; Pietrogiacomi, D.; Di Michele, A.; Rossetti, I. Photoreforming of Glucose over CuO/TiO_2. *Catalysts* **2020**, *10*, 477. [CrossRef]
104. Al-Madanat, O.; AlSalka, Y.; Ramadan, W.; Bahnemann, D.W. TiO_2 Photocatalysis for the Transformation of Aromatic Water Pollutants into Fuels. *Catalysts* **2021**, *11*, 317. [CrossRef]
105. Akhlaghi, N.; Najafpour-Darzi, G. A comprehensive review on biological hydrogen production. *Int. J. Hydrogen Energy* **2020**, *45*, 22492–22512. [CrossRef]

106. Christopher, F.C.; Kumar, P.S.; Vo, D.-V.N.; Joshiba, G.J. A review on critical assessment of advanced bioreactor options for sustainable hydrogen production. *Int. J. Hydrogen Energy* **2021**. [CrossRef]
107. Dahiya, S.; Chatterjee, S.; Sarkar, O.; Venkata Mohan, S. Renewable hydrogen production by dark-fermentation: Current status, challenges and perspectives. *Biores. Technol.* **2021**, *321*, 124354. [CrossRef]
108. Castello, E.; Nunes Ferraz-Junior, A.D. Stability problems in the hydrogen production by dark fermentation: Possible causes and solutions. *Renew. Sust. Energ. Rev.* **2020**, *119*, 109602. [CrossRef]
109. García-Depraect, O.; Munoz, R.; Rodríguez, E.; Rene, E.R.; Leon-Becerril, E. Microbial ecology of a lactate-driven dark fermentation process producing hydrogen under carbohydrate-limiting conditions. *Int. J. Hydrogen Energy* **2021**. [CrossRef]
110. Dauptain, K.; Trably, E.; Santa-Catalina, G.; Bernet, N.; Carrere, H. Role of indigenous bacteria in dark fermentation of organic substrates. *Biores. Technol.* **2020**, *313*, 123665. [CrossRef]
111. Song, W.; Ding, L.; Liu, M.; Cheng, J.; Zhou, J.; Li, Y.Y. Improving biohydrogen production through dark fermentation of steam-heated acid pretreated Alternanthera philoxeroides by mutant Enterobacter aerogenes ZJU1. *Sci. Total Environ.* **2020**, *716*, 134695. [CrossRef]
112. Li, X.; Guo, L.; Liu, Y.; Wang, Y.; She, Z.; Gao, M.; Zhao, Y. Effect of salinity and pH on dark fermentation with thermophilic bacteria pretreated swine wastewater. *J. Environ. Manag.* **2020**, *271*, 111023. [CrossRef] [PubMed]
113. Atilano-Camino, M.M.; Luévano-Montaño, C.D.; García-González, A.; Olivo-Alani, D.S.; Álvarez-Valencia, L.H.; García-Reyes, R.B. Evaluation of dissolved and immobilized redox mediators on dark fermentation: Driving to hydrogen or solventogenic pathway. *Biores. Technol.* **2020**, *317*, 123981. [CrossRef]
114. Liu, X.; He, D. Freezing in the presence of nitrite pretreatment enhances hydrogen production from dark fermentation of waste activated sludge. *J. Clean. Prod.* **2020**, *248*, 119305. [CrossRef]
115. Zhang, Y.; Xiao, L.; Hao, Q.; Li, X.; Liu, F. Ferrihydrite Reduction Exclusively Stimulated Hydrogen Production by Clostridium with Community Metabolic Pathway Bifurcation. *Acs Sustain. Chem. Eng.* **2020**, *8*, 7574–7580. [CrossRef]
116. Moura, A.G.L.; Rabelo, C.A.B.S.; Okino, C.H.; Maintinguer, S.I.; Silva, E.L.; Varesche, M.B.A. Enhancement of Clostridium butyricum hydrogen production by iron and nickel nanoparticles: Effects on hydA expression. *Int. J. Hydrogen Energy* **2020**, *45*, 28447–28461. [CrossRef]
117. Rambabu, K.; Bharath, G.; Thanigaivelan, A.; Das, D.B.; Loke Show, P.; Banat, F. Augmented biohydrogen production from rice mill wastewater through nano-metal oxides assisted dark fermentation. *Biores. Technol.* **2021**, *319*, 124243. [CrossRef]
118. Sim, Y.-B.; Jung, J.-H.; Park, J.-H.; Bakonyi, P.; Kim, S.-H. Effect of shear velocity on dark fermentation for biohydrogen production using dynamic membrane. *Biores. Technol.* **2020**, *308*, 123265. [CrossRef] [PubMed]
119. Hitam, C.N.C.; Jalil, A.A. A review on biohydrogen production through photo-fermentation of lignocellulosic biomass. *Biomass Convers. Biorefin.* **2020**. [CrossRef]
120. Baeyens, J.; Zhang, H.; Nie, J.; Appels, L.; Dewil, R.; Ansart, R.; Deng, Y. Reviewing the potential of bio-hydrogen production by fermentation. *Renew. Sust. Energ. Rev.* **2020**, *131*, 110023. [CrossRef]
121. Zhang, Z.; Zhang, H.; Li, Y.; Lu, C.; Zhu, S.; He, C.; Ai, F.; Zhang, Q. Investigation of the interaction between lighting and mixing applied during the photo-fermentation biohydrogen production process from agricultural waste. *Biores. Technol.* **2020**, *312*, 123570. [CrossRef] [PubMed]
122. Zhu, S.; Zhang, Z.; Zhang, H.; Jing, Y.; Li, Y.; Zhang, Q. Rheological properties of corn stover hydrolysate and photo-fermentation bio-hydrogen producing capacity under intermittent stirring. *Int. J. Hydrogen Energy* **2020**, *45*, 3721–3728. [CrossRef]
123. Znad, H.; Al-Mohammedawi, H.; Awual, M.R. Integrated pre-treatment stage of biosorbent—sonication for mixed brewery and restaurant effluents to enhance the photo-fermentative hydrogen production. *Biomass Bioenergy* **2021**, *144*, 105899. [CrossRef]
124. Jiang, D.; Zhang, X. Insights into correlation between hydrogen yield improvement and glycerol addition in photo-fermentation of Arundo donax L. *Biores. Technol.* **2021**, *321*, 124467. [CrossRef]
125. Zhang, H.; Li, J.; Zhang, Q.; Zhu, S.; Yang, S.; Zhang, Z. Effect of Substrate Concentration on Photo-Fermentation Bio-Hydrogen Production Process from Starch-Rich Agricultural Leftovers under Oscillation. *Sustainability* **2020**, *12*, 2700. [CrossRef]
126. Jiang, D.; Ge, X.; Zhang, T.; Chen, Z.; Zhang, Z.; He, C.; Zhang, Q.; Li, Y. Effect of alkaline pretreatment on photo-fermentative hydrogen production from giant reed: Comparison of NaOH and $Ca(OH)_2$. *Biores. Technol.* **2020**, *304*, 123001. [CrossRef] [PubMed]
127. Liu, H.; Zhang, Z.; Zhang, H.; Lee, D.-J.; Zhang, Q.; Lu, C.; He, C. Evaluation of hydrogen yield potential from Chlorella by photofermentation under diverse substrate concentration and enzyme loading. *Biores. Technol.* **2020**, *303*, 122956. [CrossRef]
128. Zhanga, Y.; Zhanga, H.; Leeb, D.-J.; Zhanga, T.; Jianga, D.; Zhanga, Z.; Zhang, Q. Effect of enzymolysis time on biohydrogen production from photofermentation by using various energy grasses as substrates. *Biores. Technol.* **2020**, *305*, 123062. [CrossRef] [PubMed]
129. Zhang, X.; Jiang, D.; Zhang, H.; Wang, Y.; Zhang, Z.; Lu, C.; Zhang, Q. Enhancement of the biohydrogen production performance from mixed substrate by photo-fermentation: Effects of initial pH and inoculation volume ratio. *Biores. Technol.* **2021**, *319*, 124153. [CrossRef]
130. Hu, J.; Yang, H.; Wang, X.; Cao, W.; Guo, L. Strong pH dependence of hydrogen production from glucose by Rhodobacter sphaeroides. *Int. J. Hydrogen Energy* **2020**, *45*, 9451–9458. [CrossRef]
131. Lu, C.; Tahir, N.; Li, W.; Zhang, Z.; Jiang, D.; Guo, S.; Wang, J.; Wang, K.; Zhang, Q. Enhanced buffer capacity of fermentation broth and biohydrogen production from corn stalk with Na_2HPO_4/NaH_2PO_4. *Biores. Technol.* **2020**, *313*, 123783. [CrossRef]

132. Guo, S.; Lu, C.; Wang, K.; Wang, J.; Zhang, Z.; Jing, Y.; Zhang, Q. Enhancement of pH values stability and photo-fermentation biohydrogen production by phosphate buffer. *Bioengineered* **2020**, *11*, 291–300. [CrossRef]
133. Hu, B.; Li, Y.; Zhu, S.; Zhang, H.; Jing, Y.; Jiang, D.; He, C.; Zhang, Z. Evaluation of biohydrogen yield potential and electron balance in the photofermentation process with different initial pH from starch agricultural leftover. *Biores. Technol.* **2020**, *305*, 122900. [CrossRef] [PubMed]
134. Lu, C.; Jing, Y.; Zhang, H.; Lee, D.-J.; Tahir, N.; Zhang, Q.; Li, W.; Wang, Y.; Liang, X.; Wang, J.; et al. Biohydrogen production through active saccharification and photofermentation from alfalfa. *Biores. Technol.* **2020**, *304*, 123007. [CrossRef] [PubMed]
135. Zhang, T.; Jiang, D.; Zhang, H.; Lee, D.-J.; Zhang, Z.; Zhang, Q.; Jing, Y.; Zhang, Y.; Xia, C. Effects of different pretreatment methods on the structural characteristics, enzymatic saccharifcation and photo-fermentative bio-hydrogen production performance of corn straw. *Biores. Technol.* **2020**, *304*, 122999. [CrossRef]
136. Al-Mohammedawi, H.H.; Znad, H. Impact of metal ions and EDTA on photofermentative hydrogen production by Rhodobacter sphaeroides using a mixture of pre-treated brewery and restaurant effluents. *Biomass Bioenergy* **2020**, *134*, 105482. [CrossRef]
137. Policastro, G.; Luongo, V.; Fabbricino, M. Biohydrogen and poly-β-hydroxybutyrate production by winery wastewater photofermentation: Effect of substrate concentration and nitrogen source. *J. Environ. Manag.* **2020**, *271*, 111006. [CrossRef]
138. Liu, C.; Shi, Y.; Liu, H.; Ma, M.; Liu, G.; Zhang, R.; Wang, W. Insight of co-fermentation of carbon monoxide with carbohydraterich wastewater for enhanced hydrogen production: Homoacetogenic inhibition and the role of pH. *J. Clean. Prod.* **2020**, *267*, 122027. [CrossRef]
139. Lee, S.H.; Lee, S.-M.; Lee, J.-H.; Lee, H.S.; Kang, S.G. Biological process for coproduction of hydrogen and thermophilic enzymes during CO fermentation. *Biores. Technol.* **2020**, *305*, 123067. [CrossRef] [PubMed]
140. Kumar, R.; Kumar, A.; Pal, A. An overview of conventional and non-conventional hydrogen production methods. *Mater. Today Proc.* **2020**. [CrossRef]
141. Kossalbayev, B.D.; Tomo, T.; Zayadan, B.K.; Sadvakasova, A.K.; Bolatkhan, K.; Alwasel, S.; Allakhverdiev, S.I. Determination of the potential of cyanobacterial strains for hydrogen production. *Int. J. Hydrogen Energy* **2020**, *45*, 2627–2639. [CrossRef]
142. Mu, D.; Liu, H.; Lin, W.; Shukla, P.; Luo, J. Simultaneous biohydrogen production from dark fermentation of duckweed and waste utilization for microalgal lipid production. *Biores. Technol.* **2020**, *302*, 122879. [CrossRef]
143. Das, S.R.; Basak, N. Molecular biohydrogen production by dark and photo fermentation from wastes containing starch: Recent advancement and future perspective. *Bioprocess Biosyst. Eng.* **2021**, *44*, 1–25. [CrossRef]
144. Mıynat, M.E.; Ören, İ.; Özkan, E.; Argun, H. Sequential dark and photo-fermentative hydrogen gas production from agar embedded molasses. *Int. J. Hydrogen Energy* **2020**, *45*, 34730–34738. [CrossRef]
145. Niño-Navarro, C.; Chairez, I.; Christen, P.; Canul-Chan, M.; García-Peña, E.I. Enhanced hydrogen production by a sequential dark and photo fermentation process: Effects of initial feedstock composition, dilution and microbial population. *Renew. Energy* **2020**, *147*, 924–936. [CrossRef]
146. Li, Y.; Zhang, Z.; Lee, D.-J.; Zhang, Q.; Jing, Y.; Yue, T.; Liu, Z. Role of L-cysteine and iron oxide nanoparticle in affecting hydrogen yield potential and electronic distribution in biohydrogen production from dark fermentation effluents by photo-fermentation. *J. Clean. Prod.* **2020**, *276*, 123193. [CrossRef]
147. Pandey, A.; Sinha, P.; Pandey, A. Hydrogen production by sequential dark and photofermentation using wet biomass hydrolysate of Spirulina platensis: Response surface methodological approach. *Int. J. Hydrogen Energy* **2021**, *46*, 7137–7146. [CrossRef]
148. Li, Y.; Zhang, Z.; Zhang, Q.; Tahir, N.; Jing, Y.; Xia, C.; Zhu, S.; Zhang, X. Enhancement of bio-hydrogen yield and pH stability in photo fermentation process using dark fermentation effluent as succedaneum. *Biores. Technol.* **2020**, *297*, 122504. [CrossRef] [PubMed]
149. Rezaeitavabe, F.; Saadat, S.; Talebbeydokhti, N.; Sartaj, M.; Tabatabaei, M. Enhancing bio-hydrogen production from food waste in single-stage hybrid dark-photo fermentation by addition of two waste materials (exhausted resin and biochar). *Biomass Bioenergy* **2020**, *143*, 105846. [CrossRef]
150. Meky, N.; Ibrahim, M.G.; Fujii, M.; Elreedy, A.; Tawfk, A. Integrated dark-photo fermentative hydrogen production from synthetic gelatinaceous wastewater via cost-effective hybrid reactor at ambient temperature. *Energy Convers. Manag.* **2020**, *203*, 112250. [CrossRef]
151. Dinesh, G.H.; Nguyen, D.D.; Ravindran, B.; Chang, S.W.; Vo, D.-V.N.; Bach, Q.-V.; Tran, H.N.; Basu, M.J.; Mohanrasu, K.; Murugan, R.S.; et al. Simultaneous biohydrogen (H_2) and bioplastic (poly-b-hydroxybutyrate-PHB) productions under dark, photo, and subsequent dark and photo fermentation utilizing various wastes. *Int. J. Hydrogen Energy* **2020**, *45*, 5840–5853. [CrossRef]
152. Li, Y.; Zhang, Z.; Xia, C.; Jing, Y.; Zhang, Q.; Li, S.; Zhu, S.; Jin, P. Photo-fermentation biohydrogen production and electrons distribution from dark fermentation effluents under batch, semi-continuous and continuous modes. *Biores. Technol.* **2020**, *311*, 123549. [CrossRef]
153. Zhang, T.; Jiang, D.; Zhang, H.; Jing, Y.; Tahir, N.; Zhang, Y.; Zhang, Q. Comparative study on bio-hydrogen production from corn stover: Photo-fermentation, dark-fermentation and dark-photo co-fermentation. *Int. J. Hydrogen Energy* **2020**, *45*, 3807–3814. [CrossRef]
154. Zhang, Y.; Yuan, J.; Guo, L. Enhanced bio-hydrogen production from cornstalk hydrolysate pretreated by alkaline-enzymolysis with orthogonal design method. *Int. J. Hydrogen Energy* **2020**, *45*, 3750–3759. [CrossRef]
155. Kannah, R.Y.; Kavitha, S.; Preethi; Karthikeyan, O.P.; Kumar, G.; Dai-Viet, N.V.; Banu, J.R. Techno-economic assessment of various hydrogen production methods—A review. *Biores. Technol.* **2021**, *319*, 124175. [CrossRef]

156. Lamy, C.; Millet, P. A critical review on the defnitions used to calculate the energy efficiency coeffcients of water electrolysis cells working under near ambient temperature conditions. *J. Power Sources* **2020**, *447*, 227350. [CrossRef]
157. Grigoriev, S.A.; Fateev, V.N.; Bessarabov, D.G.; Millet, P. Current status, research trends, and challenges in water electrolysis science and technology. *Int. J. Hydrogen Energy* **2020**, *45*, 26036–26058. [CrossRef]
158. Zhou, D.; Li, P.; Xu, W.; Jawaid, S.; Mohammed-Ibrahim, J.; Liu, W.; Kuang, Y.; Sun, X. Recent Advances in Non-Precious Metal-Based Electrodes for Alkaline Water Electrolysis. *ChemNanoMat* **2020**, *6*, 336–355. [CrossRef]
159. Krishnan, S.; Fairlie, M.; Andres, P.; de Groot, T.; Kramer, G.J. Power to gas (H_2): Alkaline electrolysis. In *Technological Learning in the Transition to a Low-Carbon Energy System*; Junginger, M., Louwen, A., Eds.; Academic Press: London, UK, 2020; pp. 165–187. [CrossRef]
160. Song, S.; Yu, L.; Xiao, X.; Qin, Z.; Zhang, W.; Wang, D.; Bao, J.; Zhou, H.; Zhang, Q.; Chen, S.; et al. Outstanding oxygen evolution reaction performance of nickel iron selenide/stainless steel mat for water electrolysis. *Mat. Today Phys.* **2020**, *13*, 100216. [CrossRef]
161. Liu, X.; Guo, R.; Kun, N.; Xia, F.; Niu, C.; Wen, B.; Meng, J.; Wu, P.; Wu, J.; Wu, X.; et al. Reconstruction-Determined Alkaline Water Electrolysis at Industrial Temperatures. *Adv. Mater.* **2020**, *32*, 2001136. [CrossRef] [PubMed]
162. Kou, T.; Wang, S.; Shi, R.; Zhang, T.; Chiovoloni, S.; Lu, J.Q.; Chen, W.; Worsley, M.A.; Wood, B.C.; Baker, S.E.; et al. Periodic Porous 3D Electrodes Mitigate Gas Bubble Trafc during Alkaline Water Electrolysis at High Current Densities. *Adv. Energy Mater.* **2020**, *10*, 2002955. [CrossRef]
163. Yang, F.; Kim, M.J.; Brown, M.; Wiley, B.J. Alkaline Water Electrolysis at 25 A cm^{-2} with a Microfbrous Flow-through Electrode. *Adv. Energy Mater.* **2020**, *10*, 2001174. [CrossRef]
164. López-Fernández, E.; Gil-Rostra, J.; Espinós, J.P.; González-Elipe, A.R.; de Lucas Consuegra, A.; Yubero, F. Chemistry and Electrocatalytic Activity of Nanostructured Nickel Electrodes for Water Electrolysis. *Acs Catal.* **2020**, *10*, 6159–6170. [CrossRef]
165. Carbone, A.; Campagna Zignani, S.; Gatto, I.; Trocino, S.; Aricò, A.S. Assessment of the FAA3-50 polymer electrolyte in combination with a $NiMn_2O_4$ anode catalyst for anion exchange membrane water electrolysis. *Int. J. Hydrogen Energy* **2020**, *45*, 9285–9292. [CrossRef]
166. Yan, X.; Yang, X.; Su, X.; Gao, L.; Zhao, J.; Hu, L.; Di, M.; Li, T.; Ruan, X.; He, G. Twisted ether-free polymer based alkaline membrane for high-performance water electrolysis. *J. Power Sources* **2020**, *480*, 228805. [CrossRef]
167. Fortin, P.; Khoza, T.; Cao, X.; Yngve Martinsen, S.; Oyarce Barnett, A.; Holdcroft, S. High-performance alkaline water electrolysis using Aemion™ anion exchange membranes. *J. Power Sources* **2020**, *451*, 227814. [CrossRef]
168. Pushkareva, I.V.; Pushkarev, A.S.; Grigoriev, S.A.; Modisha, P.; Bessarabov, D.G. Comparative study of anion exchange membranes for low-cost water electrolysis. *Int. J. Hydrogen Energy* **2020**, *45*, 26070–26079. [CrossRef]
169. Hegge, F.; Lombeck, F.; Cruz Ortiz, E.; Bohn, L.; von Holst, M.; Kroschel, M.; Hübner, J.; Breitwieser, M.; Strasser, P.; Vierrath, S. Efficient and Stable Low Iridium Loaded Anodes for PEM Water Electrolysis Made Possible by Nanofiber Interlayers. *ACS Appl. Energy Mater.* **2020**, *3*, 8276–8284. [CrossRef]
170. Klose, C.; Saatkamp, T.; Münchinger, A.; Bohn, L.; Titvinidze, G.; Breitwieser, M.; Kreuer, K.-D.; Vierrath, S. All-Hydrocarbon MEA for PEM Water Electrolysis Combining Low Hydrogen Crossover and High Effciency. *Adv. Energy Mater.* **2020**, *10*, 1903995. [CrossRef]
171. Siracusano, S.; Trocino, S.; Briguglio, N.; Panto, F.; Arico, A.S. Analysis of performance degradation during steady-state and load-thermal cycles of proton exchange membrane water electrolysis cells. *J. Power Sources* **2020**, *468*, 228390. [CrossRef]
172. Kang, Z.; Alia, S.M.; Young, J.L.; Bender, G. Effects of various parameters of different porous transport layers in proton exchange membrane water electrolysis. *Electrochim. Acta* **2020**, *354*, 136641. [CrossRef]
173. Lopata, J.; Kang, Z.; Young, J.; Bender, G.; Weidner, J.W.; Shimpalee, S. Effects of the Transport/Catalyst Layer Interface and Catalyst Loading on Mass and Charge Transport Phenomena in Polymer Electrolyte Membrane Water Electrolysis Devices. *J. Electrochem. Soc.* **2020**, *167*, 064507. [CrossRef]
174. Schuler, T.; Ciccone, J.M.; Krentscher, B.; Marone, F.; Peter, C.; Schmidt, T.J.; Büchi, F.N. Hierarchically Structured Porous Transport Layers for Polymer Electrolyte Water Electrolysis. *Adv. Energy Mater.* **2020**, *10*, 1903216. [CrossRef]
175. Huang, J.; Xie, Y.; Yan, L.; Wang, B.; Kong, T.; Dong, X.; Wang, Y.; Xia, Y. Decoupled amphoteric water electrolysis and its integration with Mn–Zn battery for flexible utilization of renewables. *Energy Environ. Sci.* **2021**, *14*, 883–889. [CrossRef]
176. Mayerhöfer, B.; McLaughlin, D.; Böhm, T.; Hegelheimer, M.; Seeberger, D.; Thiele, S. Bipolar Membrane Electrode Assemblies for Water Electrolysis. *ACS Appl. Energy Mater.* **2020**, *3*, 9635–9644. [CrossRef]
177. Tucker, M.C. Progress in metal-supported solid oxide electrolysis cells: A review. *Int. J. Hydrogen Energy* **2020**, *45*, 24203–24218. [CrossRef]
178. Leia, L.; Zhang, J.; Guan, R.; Liu, J.; Chen, F.; Tao, Z. Energy storage and hydrogen production by proton conducting solid oxide electrolysis cells with a novel heterogeneous design. *Energy Conv. Manag.* **2020**, *218*, 113044. [CrossRef]
179. Trini, M.; Hauch, A.; De Angelis, S.; Tong, X.; Vang Hendriksen, P.; Chen, M. Comparison of microstructural evolution of fuel electrodes in solid oxide fuel cells and electrolysis cells. *J. Power Sources* **2020**, *450*, 227599. [CrossRef]
180. Teng, Z.; Xiao, Z.; Yang, G.; Guo, L.; Yang, X.; Ran, R.; Wang, W.; Zhou, W.; Shao, Z. Efficient water splitting through solid oxide electrolysis cells with a new hydrogen electrode derived from A-site cation-deficient $La_{0.4}Sr_{0.55}Co_{0.2}Fe_{0.6}Nb_{0.2}O_{3-d}$ perovskite. *Mater. Today Energy* **2020**, *17*, 100458. [CrossRef]

181. Kamlungsua, K.; Su, P.-C. Moisture-dependent electrochemical characterization of $Ba_{0.2}Sr_{1.8}Fe_{1.5}Mo_{0.5}O_{6-d}$ as the fuel electrode for solid oxide electrolysis cells (SOECs). *Electrochim. Acta* **2020**, *355*, 136670. [CrossRef]
182. Prasopchokkul, P.; Seeharaj, P.; Kim-Lohsoontorn, P. $Ba_{0.5}Sr_{0.5}(Co_{0.8}Fe_{0.2})_{1-x}Ta_xO_{3-d}$ perovskite anode in solid oxide electrolysis cell for hydrogen production from high-temperature steam electrolysis. *Int. J. Hydrogen Energy* **2021**, *46*, 7023–7036. [CrossRef]
183. Rajendran, S.; Thangavel, N.K.; Ding, H.; Ding, Y.; Ding, D.; Reddy Arava, L.M. Tri-Doped $BaCeO_3-BaZrO_3$ as a Chemically Stable Electrolyte with High Proton-Conductivity for Intermediate Temperature Solid Oxide Electrolysis Cells (SOECs). *ACS Appl. Mater. Interfaces* **2020**, *12*, 38275–38284. [CrossRef]
184. Tong, X.; Ovtar, S.; Brodersen, K.; Vang Hendriksen, P.; Chen, M. Large-area solid oxide cells with $La_{0.6}Sr_{0.4}CoO_{3-\delta}$ infiltrated oxygen electrodes for electricity generation and hydrogen production. *J. Power Sources* **2020**, *451*, 227742. [CrossRef]
185. Bernadet, L.; Moncasi, C.; Torrell, M.; Tarancón, A. High-performing electrolyte-supported symmetrical solid oxide electrolysis cells operating under steam electrolysis and co-electrolysis modes. *Int. J. Hydrogen Energy* **2020**, *45*, 14208–14217. [CrossRef]
186. Temluxame, P.; Puengjinda, P.; Peng-ont, S.; Ngampuengpis, W.; Sirimungkalakul, N.; Jiwanuruk, T.; Sornchamni, T.; Kim-Lohsoontorn, P. Comparison of ceria and zirconia based electrolytes for solid oxide electrolysis cells. *Int. J. Hydrogen Energy* **2020**. [CrossRef]
187. Varela, C.; Mostafa, M.; Zondervan, E. Modeling alkaline water electrolysis for power-to-x applications: A scheduling approach. *Int. J. Hydrogen Energy* **2021**. [CrossRef]
188. Sun, Z.; Wang, G.; Koh, S.W.; Ge, J.; Zhao, H.; Hong, W.; Fei, J.; Zhao, Y.; Gao, P.; Miao, H.; et al. Solar-Driven Alkaline Water Electrolysis with Multifunctional Catalysts. *Adv. Funct. Mater.* **2020**, *30*, 2002138. [CrossRef]
189. Mastropasqua, L.; Pecenati, I.; Giostri, A.; Campanari, S. Solar hydrogen production: Techno-economic analysis of a parabolic dishsupported high-temperature electrolysis system. *Appl. Energy* **2020**, *261*, 114392. [CrossRef]
190. Milewski, J.; Kupecki, J.; Szczęśniak, A.; Uzunow, N. Hydrogen production in solid oxide electrolyzers coupled with nuclear reactors. *Int. J. Hydrogen Energy* **2020**. [CrossRef]